High-content high-resolution microscopy and deep learning assisted analysis reveals host and bacterial heterogeneity during *Shigella* infection.

Ana T. López-Jiménez*, Dominik Brokatzky, Kamla Pillay, Tyrese Williams, Gizem Özbaykal Güler and Serge Mostowy*.

* Corresponding authors: ana.lopezjimenez@lshtm.ac.uk, serge.mostowy@lshtm.ac.uk

Department of Infection Biology, London School of Hygiene and Tropical Medicine, Keppel Street, London WC1E 7HT, United Kingdom

Keywords: heterogeneity, high-content imaging, deep learning, septins, *Shigella*.

Abstract

Shigella flexneri is a Gram-negative bacterial pathogen and causative agent of bacillary dysentery. *S. flexneri* is closely related to *Escherichia coli* but harbors a virulence plasmid that encodes a Type III Secretion System (T3SS) required for host cell invasion. Widely recognized as a paradigm for research in cellular microbiology, *S. flexneri* has emerged as important to study mechanisms of cell-autonomous immunity, including septin cage entrapment. Here we use high-content high-resolution microscopy to monitor the dynamic and heterogeneous *S. flexneri* infection process by assessing multiple host and bacterial parameters (DNA replication, protein translation, T3SS activity). In the case of infected host cells, we report a reduction in DNA and protein synthesis together with morphological changes that suggest *S. flexneri* can induce cell-cycle arrest. We developed an artificial intelligence image analysis approach using Convolutional Neural Networks to reliably quantify, in an automated and unbiased manner, the

recruitment of SEPT7 to intracellular bacteria. We discover that heterogeneous SEPT7 assemblies are recruited to bacteria with increased T3SS activation. Our automated microscopy workflow is useful to illuminate diverse host and bacterial interactions at the single-cell and population level, and to fully characterise the intracellular microenvironment controlling the *S. flexneri* infection process.

Introduction

Shigella flexneri is a Gram-negative bacterium and the etiologic agent of bacillary dysentery, an intestinal infectious disease that kills more than 150 thousand people worldwide per year, disproportionally affecting children under 5 years old from low- and middle-income countries (Global Burden of Disease Collaborative Network., 2020). After the ingestion of a small number of bacteria (10-100), *S. flexneri* rapidly colonises the human intestinal epithelium. For this, *S. flexneri* uses a Type 3 Secretion System (T3SS) that injects bacterial effectors into the host cell to modulate key aspects of the infection process and to evade innate immune defences by the host (Schnupf & Sansonetti, 2019). Following uptake by host cells, *S. flexneri* breaks its vacuolar compartment to access the cytosol (Ray et al., 2010). Here, the virulence factor IcsA enables *S. flexneri* to hijack host actin and polymerise comet tails that render bacteria motile to disseminate to neighbouring cells and spread in the tissue (Bernardini et al., 1989; Egile et al., 1999).

Septins are highly-conserved GTP-binding proteins that form heteromeric complexes (hexamers, octamers) that assemble into non-polar filaments, bundles and rings (Martins et al., 2023; Soroor et al., 2021; Szuba et al., 2021; Woods & Gladfelter, 2021). Septins are involved in many physiological cellular processes (eg. cytokinesis, cilia formation), and play key roles during infection (Mostowy & Cossart, 2012; Robertin & Mostowy, 2020; Spiliotis & Nakos, 2021). Septins form collar-like structures at the plasma membrane during bacterial invasion (Boddy et al., 2018; Mostowy et al., 2009; Robertin et al., 2023), and ring-like structures surrounding membrane protrusions in cell-to-cell bacterial spread (Mostowy et al., 2010). In the cytosol septins are recruited to actin-polymerising bacteria, including *S. flexneri* and *Mycobacterium marinum*, as cage-like structures (Mostowy et al., 2010). In the case of *S. flexneri*, septins are recruited to μm-scale curvature at bacterial poles and the division site, which are enriched in the negatively charged phospholipid cardiolipin (Krokowski et al., 2018).

Recent work has shown that IcsA promotes the recruitment of septins to *S. flexneri*, and that lipopolysaccharide (LPS) inhibits *S. flexneri*-septin cage entrapment (Lobato-Márquez et al., 2021; Mostowy et al., 2010). Septin cages prevent bacterial actin tail motility and therefore are considered as an antibacterial mechanism of host defence (Krokowski et al., 2018; Mostowy et al., 2010).

Intracellular infection is usually portrayed as a uniform, synchronised and highly orchestrated process. However, infection assays performed in controlled laboratory environments with isogenic populations display a high level of complexity (Avraham et al., 2015; Toniolo et al., 2021). It is particularly unknown how different subsets of bacteria (eg. motile vs. non motile bacteria) can colonise distinct intracellular microenvironments and become targeted by multiple cell-autonomous immunity mechanisms (eg. septin cages, autophagy). It has been proposed that this diversity of intracellular niches impacts bacterial physiology (Day et al., 2023; Gutierrez & Enninga, 2022; Santucci et al., 2021). For example, it may affect individual bacterial ability to acquire nutrients, to be exposed to varying antibiotic concentrations, or to elicit different responses and signalling pathways within the host cell. While the concept of phenotypic heterogeneity in prokaryotic clonal populations is well established (Ackermann, 2015), the concept is emerging also in eukaryotic cells where non genetic differences may for instance explain individual cell sensitivity and responses by cell-autonomous immunity (McDonald & Dedhar, 2024). In addition, previous high-content studies coupled with mathematical modelling have shown that host cell context (including local cell density, lipid composition at the plasma membrane, or previous infection status) affects their susceptibility to viral and bacterial infection (Snijder et al., 2009; Voznica et al., 2018). It is therefore paramount to study host and bacterial cells at the single-cell level, to assess the individual responses that collectively contribute to the infection process.

Here, to dissect the complexity of *S. flexneri* infection in epithelial cells, we use high-content high-resolution microscopy coupled to automated image analysis. High-content microscopy enables the automated acquisition of thousands of microscopy images and therefore is useful to capture the heterogeneity of individual host and bacterial cells during the infection process for quantitative analysis (Aylan et al., 2023; Brodin & Christophe, 2011; Deboosere et al., 2021; Dramé et al., 2023; Fisch et al., 2019a; Lensen et al., 2023; Pylkkö et al., 2021). We analyse multiple parameters, such as morphological host cell features, the *de novo* synthesis of DNA and proteins in both host and bacterial cells, as well as activation of the bacterial T3SS. To investigate the antimicrobial potential of septin-mediated immunity, we develop a deep-learning based approach to automatically identify septin-*S. flexneri* interactions. Together, we highlight the power of high-content microscopy and artificial intelligence to reveal insights on both host and bacterial cells, and illuminate fundamental biology underlying the *S. flexneri* infection process.

Results

Capturing the heterogeneity of *S. flexneri* infection using high-content microscopy.

To understand the complexity and reveal the heterogeneity of *S. flexneri* infection in human epithelial cells, we dissected the infection process using high-content high-resolution microscopy and HeLa cell infection model (**Figure 1A, B, Figure 1-figure supplement 1A**). We observed a mean of 11.5% of infected cells measured by fluorescence at 3h 40 min post infection (hpi) at MOI 100:1 (**Figure 1C**). These infected cells presented different burdens of bacteria following an exponential decay distribution (**Figure 1D**), reflective of the formation of infection foci (Ortega et al., 2019). With growing evidence of the cytosol being a non-homogeneous compartment containing concentration gradients, biomolecular condensates, protein complexes and concentrates (van Tartwijk & Kaminski, 2022), we tested whether *S. flexneri* may be exposed to different intracellular microenvironments. For this, we measured the distance of bacteria to the centroid of cells (**Figure 1E**) and observed a median distance of 8.74 µm. The median distance to the centroid of the cell significantly decreased with increasing bacterial burden (**Figure 1E**), suggesting that the microenvironment of bacteria is diverse and changes as bacteria replicate intracellularly and populate the central parts of host cytosol after uptake at the host cell periphery. To dissect the heterogeneity in host cells, we quantified an increase of 36.9% and 22.3% in the cellular and nuclear area of infected cells, respectively (**Figure 1G, I**), which was dependent on the infection burden (**Figure 1H, J**). In addition, the total amount of Hoechst fluorescence in the cell nucleus increased 29.4% in infected cells (**Figure 1-figure supplement 1B**), indicating either an increase in nuclear volume or altered chromatin condensation. To test if this effect was due to morphological rearrangements during infection, we treated cells with Latrunculin B to inhibit actin polymerisation. While cells treated with Latrunculin B decreased their cellular area (but not their nuclear area) (**Figure 1-figure supplement 1C, D**), the drug did not abrogate the difference in size between infected

and uninfected cells. Taken together, these results highlight profound morphological rearrangements during infection that are dependent on the infection burden.

Epithelial cells reduce *de novo* DNA and protein synthesis upon infection.

In order to understand the physiological state of enlarged epithelial cells infected with *S. flexneri*, we monitored host DNA replication and protein translation using Click-chemistry. Using a 1 h pulse of the clickable thymidine analogue Edu, we specifically visualized and quantified *de novo* DNA synthesis in the population of epithelial cells with high-content microscopy (**Figure 2A, Figure 2-figure supplement 1**). We identified the subpopulation of cells in S-phase by their high level of Edu incorporation. Consistent with this, this subpopulation of cells was fully abrogated in the presence of the S-phase blocker Aphidicolin (Pedrali-Noy et al., 1980) (**Figure 2-figure supplement 2A, B**). Approximately one third of uninfected cells (34.45%) were found in S-phase (**Figure 2B, C**), in agreement with S-phase lasting around one third of the cell cycle (~8h out of ~22h). Infected cells presented a similar proportion of cells in S-phase (35.89%), indicating that *S. flexneri* infection did not block transition of cells from G1 to S at the timepoint tested. We then assessed the amount of *de novo* DNA synthesis incorporated in cells in S-phase during infection. Surprisingly, we observed a reduction of Edu incorporation in infected cells (**Figure 2D**), which was dependent on the bacterial burden (**Figure 2E**). These results indicate that *S. flexneri* infection slows down DNA synthesis of epithelial cells.

To assess protein translation, we used a 1h pulse of the clickable methionine analogue AHA, which specifically labels *de novo* synthesized proteins as AHA incorporation is reduced after treatment with the inhibitor of translational elongation Cycloheximide (Ennis & Lubin, 1964) (**Figure 2-figure supplement 1C, D**). During infection, we observed a reduction of protein

translation in infected cells compared to non-infected cells (**Figure 2F,G**), which was also dependent on the bacterial burden (**Figure 2H**).

Collectively, the cell morphological rearrangements together with the reduction of *de novo* DNA and protein synthesis in infected epithelial cells suggests that *S. flexneri* induces an arrest in the host cell cycle.

Design of a deep learning pipeline to automatically identify bacteria interacting with SEPT7.

S. flexneri have been shown to interact with septins during infection. These interactions include septin ring-like structures surrounding phagocytic cups, autophagosomes, actin tails and protrusions, all being morphologically diverse structures that are normally scored by hand (Krokowski et al., 2018; Lobato-Márquez et al., 2023; Mostowy et al., 2010) . To study septin-associated bacteria using high-content microscopy, we designed a tailored analysis pipeline for the automatic and unbiased identification of SEPT7-bacteria interactions (**Figure 3**). SEPT7 is a core component of septin hexamers and octamers, and is historically used to identify septin structures (Mostowy et al., 2010). The analysis pipeline includes two deep learning models based on Convolutional Neural Networks (CNN), which are effective in solving classification tasks in computer vision (Krizhevsky et al., n.d.; Lecun et al., 2015; Nielsen, 2015). As septins can surround individual and also multiple bacteria simultaneously (**Figure 4-figure supplement 1A**), we focused on individual bacteria. For this, we trained the first classification model to discriminate between “single” bacteria and “clumps”. The second classification model was designed to assign those single bacteria into “SEPT7-positive structures” or alternatively “negatives”, according to the morphology of SEPT7 recruitment around them.

The first classification model (discerning “single” versus “clumped” bacteria) together with its training and performance metrics is summarized in **Figure 4**. A large dataset of annotated

bacteria (**Figure 4A, B, Figure 4-figure supplement 1B**) was used to train a Sequential model with a typical CNN architecture that was experimentally tested and optimised accordingly for best results (**Figure 4C**). This model provided a good fit of the training data (high accuracy, low loss), with similar predictive power for the validation dataset (**Figure 4D, E**). Performance of the model was further assessed with a confusion matrix where a separate annotated test dataset was challenged and correct number of predictions scored, showing that 96% of SEPT7 structures and 83% of clumps were correctly identified (**Figure 4F**). Finally, effective performance of the model was ensured with high values achieved in additional metrics testing for type I and II errors (precision, recall, F1-score) (**Figure 4G**).

The second classification task (identification of SEPT7 "positive" vs "negative" bacteria) was more challenging due to their intrinsic heterogeneity plus the presence of ubiquitious SEPT7 filaments that populate the vicinity of bacteria (but do not associate with bacteria per se). To address these challenges, we increased the amount of data and complexity of the second classification model (**Figure 4H-J, Figure 4-figure supplement 1C**) compared to the first (**Figure 4A-C**). This included more than 1200 images of *S. flexneri* associated to SEPT7, both from infections with wild-type bacteria or expressing AfaI to increase bacterial invasion. The training process achieved a high accuracy and low loss for the training and validation dataset (**Figure 4K, L**). Correct prediction of manually annotated SEPT7 positive structures was 80% as shown in the confusion matrix (**Figure 4M**), with performance metrics Precision, Recall and F1 score also around 0.8 (**Figure 4N**).

Characterization of the morphological heterogeneity of SEPT7 recruitment to *S. flexneri*.

The training of the classification model to identify bacteria associated to SEPT7 required a large dataset of images. We observed diverse morphological patterns of SEPT7 signal around bacteria (**Figure 5 A-C**). We differentiated five frequent subcategories from a total of 855

cases. The first corresponds to most cases (66.7%), where SEPT7 forms rings that entrap bacteria transversally (**Figure 5A, B, a**). We also observed two categories where SEPT7 surrounds bacteria more homogeneously either in a tight (18.2%) or loose association (6.1%) (**Figure 5A, B, b-c**). Finally, we observed partial SEPT7 recruitment, with only one (5.0%) or two (4.0%) bacterial poles being targeted (**Figure 5A, B, d-e**). Given this diversity, we combined the entire dataset to summarise the probability of SEPT7 interactions with bacteria (**Figure 5-figure supplement 1**). As bacteria are found in any orientation inside epithelial cells, we included only those instances where the z-projection of the bacterial axis measured more than 2.5µm, ensuring they were positioned horizontally when imaged. Representations shown in **Figure 5-figure supplement 1A, C** and graphs in **Figure 5-figure supplement 1B, D** can be understood as a probability map of the area of influence of SEPT7 when associating with intracellular *S. flexneri*.

SEPT7 is recruited to *S. flexneri* with increased T3SS activity.

Septins have previously been shown to recognise growing bacterial cells *in vitro* and during infection of HeLa cells, using pharmacologic and genetic manipulation (Krokowski et al., 2018; Lobato-Márquez et al., 2021). To test the metabolic state of SEPT7-associated *S. flexneri* at 3h 40 min post infection (hpi) we used our high-content imaging and analysis pipeline (**Figure 6**). We measured *S. flexneri de novo* synthesis of DNA and proteins using a 1 h pulse Click-IT Edu and Click-IT AHA. Only active bacteria incorporated these analogues, as the antibiotic Nalidixic acid (inhibitor of the bacterial DNA gyrase (Sugino et al., 1977)) and Rifampicin (inhibitor of the bacterial RNA polymerase (Ezekiel & Hutchins, 1968)) significally reduced their incorporation, respectively (**Figure 6-figure supplement 1A-D, Figure 6-figure supplement 1E,F)**. During infection, bacteria associated with SEPT7 showed heterogeneus

levels of DNA synthesis and protein translation similar to SEPT7-negative bacteria (**Figure 6A-H**).

S. flexneri pathogenicity relies on its T3SS. To understand effector secretion at the individual bacterial level, we used *S. flexneri* expressing the Transcription-based Secretion Activity Reporter (TSAR) (Campbell-Valois et al., 2014). This reporter comprises a short lived fast-maturing superfolder GFP (GFPmsf2) that is expressed in conditions where the T3SS is active, such as in broth upon addition of congo red (**Figure 7-figure supplement 1A, B**) (Parsot et al., 1995) and during infection (**Figure 7**). We observed heterogeneity in TSAR signal (**Figure 7A,B**). T3SS activation was higher in bacteria found in cells with a low bacterial burden (less than 10 intracellular bacteria) (**Figure 7A,C**). This suggests the highest level of activation occurs in bacterial pioneers that colonise neighbouring cells, in agreement with previous reports (Campbell-Valois et al., 2014). We then assessed T3SS activation in *S. flexneri* associated with SEPT7 using our deep learning analysis pipeline (**Figure 7D-H**). We detected a significant increase in TSAR-positive bacteria in SEPT7 associated *S. flexneri* compared to SEPT7-negative bacteria (**Figure 7G,H**). These include SEPT7-associated protrusions and cage-like structures (**Figure 7E**, **Figure 7-figure supplement 1C**). These data underscore the antimicrobial role of septins in associating with actively secreting bacteria.

Discussion

Unravelling the intrinsic heterogeneity of host and bacterial cells underlying the infection process is paramount to design effective therapeutic strategies. High-content and high-throughput image analysis are ideal tools to capture this heterogeneity when coupled to automatic phenotypic image analysis (Eliceiri et al., 2012; Mattiazzi Usaj et al., 2016; Pegoraro & Misteli, 2017). Here we use high-content high-resolution microscopy and automated image

analysis to quantitatively dissect the heterogeneity of *S. flexneri* in epithelial cells at the single-cell and population level at unprecedented subcellular detail.

We discover that *S. flexneri* induces important morphological and physiological changes in epithelial cells after 3h40min post infection. These include a marked decrease of DNA synthesis in cells in S-phase. Consistent with the ability of bacteria to manipulate the host cell cycle, *S. flexneri* has been shown to induce genotoxic stress (Bergounioux et al., 2012) and block the G2/M phase transition (Iwai et al., 2007; Wang et al., 2019). We also observed a collective shutdown of protein expression, which happened in a bacterial-burden dependent manner. A recent report has shown that the OspC family of *S. flexneri* effectors ADP-riboxanates the host translation initiation factor 3, leading to translational arrest and the formation of stress granules (Zhang et al., 2024). Collectively, these observations suggest that *S. flexneri* infection induces host cell stress and arrests the progression of the cell cycle. In the natural *S. flexneri* niche of the human gut, such an arrest would prevent maturation and shedding of infected epithelial cells, thereby promoting efficient gut colonisation (Iwai et al., 2007).

To understand how bacteria are targeted by cell-autonomus immune defences, such as septin cage entrapment, it is necessary to investigate phenotypic characteristics of targeted bacteria and the heterogeneous recruitment of cell-autonomous immune factors. While traditional image segmentation tools fail to enable this task, rapidly evolving developments in the field of computer vision are democratising the use of deep learning and CNNs for multiple applications (Berg et al., 2019; Hung et al., 2020; Stringer et al., 2020; von Chamier et al., 2021; Weigert et al., 2020) including infection biology (Davidson et al., 2021; Fisch et al., 2019b, 2021; Touquet et al., 2018). However, the analysis of complex datasets still requires a tailored approach, as shown here for bacterial interactions with the septin cytoskeleton (which is ubiquitious in the cell and forms diverse assemblies whose precise identification requires high resolution). We

successfully implement a CNN based approach for the automated classification of bacteria associated with SEPT7 assemblies using z-stacks projections, enabling the analysis of thousands of bacterial cells while saving time and preventing human bias. Building upon this work, future studies will improve use of 3D data for CNN re-training instead of z-stack projections, to allow more precise identification of *S. flexneri*-septin interactions, particularly when bacteria are placed perpendicular to the imaging plane.

A large dataset of images depicting *S. flexneri* – SEPT7 interactions was acquired to train the deep learning algorithm and to characterize the diversity of these structures. We observe that the most frequent septin assembly is in the form of rings transversally surrounding the bacterial surface. We also detected alternative morphologies, including homogeneous SEPT7 labelling surrounding the bacterial surface (tight vs loose), as well as the discrete recruitment of SEPT7 to one or two bacterial poles. While previous work has shown that septin cage assembly around *S. flexneri* can start with the discrete recruitment of septins to one or two bacterial poles (Krokowski et al., 2018), it is not yet known if the different septin assemblies we describe here correspond to different stages or fates of the same structure or whether it marks separate biological events. To fully address this question, follow-up studies should include timelapse analysis of septin cage formation. We use deep learning analysis to interrogate intracellular bacteria and show that *S. flexneri* associated with SEPT7 present heterogenous DNA and protein synthesis. In addition, we show that bacteria associated with SEPT7 have increased T3SS activity (as compared to bacteria not associated with SEPT7). T3SS activity has been shown to be higher in motile bacteria (Campbell-Valois et al., 2014) which reinforces the antimicrobial role of septins in counteracting actin tail motility. Altogether, our deep learning tool to analyse septin-bacteria interactions opens the door to future studies on interactions between bacteria and components of cell-autonomous immunity.

Concluding remarks

Heterogeneity in a controlled lab environment is only a small representation of the broader heterogeneity underlying the clinical infection process, considering the genetic background of the patient, interactions with microbiota, etc. In the future, our pipeline can be applied to investigate septin-bacteria interactions among different *Shigella* spp. or clinically relevant strains, as well as other intracellular bacteria (eg. *M. marinum*, *Staphylococcus aureus*, *Pseudomonas aeruginosa*). In addition, our pipeline can be adapted to identify and score other cytoskeletal structures (such as actin tails) or membrane organelles (such as autophagosomes) associated with intracellular bacteria. Ultimately, we envision that our automated microscopy workflows will help to screen pharmacologic or genetic libraries in a multiparametric manner and understand their impact on host and bacterial cells at the single-cell and population level. In this way, novel host and bacterial factors underlying heterogeneity and bacterial pathogenesis could be identified, leading to transformative therapeutic strategies to combat bacterial infection in humans.

Materials and methods

Key Resources Table				
Reagent type (species) or resource	**Designation**	**Source or reference**	**Identifiers**	**Additional information**
gene (*Drosophila melanogaster*)	nito	GenBank	FLYB:FBgn0027548	
strain, strain background (*Escherichia coli*)	BL21(DE3)	Sigma-Aldrich	CMC0016	Electrocompetent cells
genetic reagent (*D. melanogaster*)	MTD-Gal4	Bloomington Drosophila Stock Center	BDSC:31777; FLYB:FBtp0001612; RRID:BDSC_31777	FlyBase symbol: P{GAL4-nos.NGT}
cell line (*D. melanogaster*)	S2	This paper	FLYB:FBtc0000181; RRID:CVCL_Z992	Cell line maintained in N. Perrimon lab; FlyBase symbol: S2-DRSC.
cell line (*Homo-sapiens*)	Dermal fibroblast (normal, Adult)	ATCC	PCS-201–012	
transfected construct (*M. musculus*)	4E-BP1 shRNA #1	VectorBuilder	Cat#LVS (VB181217-1124dqm)-C	Lentiviral construct to transfect and express the shRNA.
transfected construct (human)	siRNA to Dynamin 2 (SMARTpool)	Dharmacon/Thermo Fisher Scientific	Huang et al., 2004	transfected construct (human)

biological sample (*Macaca fascicularis*)	Primary simian hepatocytes	SingHealth, Singapore		Freshly isolated from Macaca fascicularis
antibody	anti-3-PGDH (Rabbit polyclonal)	Millipore	Cat# ABS571, RRID:AB_2783876	IF(1:1000), WB (1:1000)
antibody	anti-CRALBP (Mouse monoclonal)	Abcam	Cat# ab15051, RRID:AB_2269474	IF(1:500)
antibody	anti-human CD235a-APC (Mouse monoclonal)	Thermo Fisher Scientific	Cat#: 17-9987-42; RRID:AB_2043823	FACS (5 ul per test)
recombinant DNA reagent	PLKO-GFP (plasmid)	This paper		GFP version of pLKO.1-Puro
recombinant DNA reagent	PLKO.1-Puro (plasmid)	Sigma-Aldrich	RRID :Addgene_10878	Pol III based shRNA backbone
sequence-based reagent	Gipc1_F	This paper	PCR primers	GGGAAAG GACAAAA GGAACCC
sequenced-based reagent	Gipc1_R	This paper	PCR primers	CAGGGCA TTTGCACC CCATGCC
sequenced-based reagent	siRNA: nontargetin control	Thermo Fisher	4390843	Silencer Select
peptide, recombinant protein	Streptavidin	Thermo Fisher	Cat. #: 434302	
commercial assay or kit	In-Fusion HD Cloning	Clontech	Clontech:639647	

chemical compound, drug	CBR-5884	Sigma Aldrich	SML1656	
software, algorithm	SPSS	SPSS	RRID:SCR_002865	
other	DAPI stain	Invitrogen	D1306	(1 µg/mL)

Reagents. The following antibodies were used: rabbit anti-SEPT7 (1:100 dilution, #18991, IBL), Alexa-488-conjugated anti-rabbit antibody (1:500, #10729174, ThermoFisher Scientific), Alexa-647-conjugated anti-rabbit antibody (1:500, #A27040, ThermoFisher Scientific). The following dyes were used: Alexa-647-conjugated phalloidin (1:500, #10656353, ThermoFisher Scientific), Hoechst (1:500, #H3570, ThermoFisher Scientific), 0.01% (w/v) congo red (#C6767, Sigma-Aldrich). The following drugs were used: 50 µg/mL aphidicolin (#A0781 Sigma-Aldrich), 50 µg/mL cycloheximide (#2112 Cell Signalling), 2 µg/mL nalidixic acid (#N8878 Sigma-Aldrich), and 100 µg/ml rifampicin (#R3501 Sigma-Aldrich).

Bacterial strains and culture conditions. The bacterial strains and plasmids described in this study are listed in **Sup. Table 1**. *Shigella flexneri* 5a str. M90T mCherry was used throughout the manuscript unless indicated otherwise unless indicated otherwise. *S. flexneri* strains were grown in trypticase soy broth (TCS) agar containing congo red to select for red colonies, indicative of a functional T3SS. Conical polypropylene tubes (#CLS430828, Corning) containing 5 ml of TCS were inoculated with individual red colonies of *S.flexneri* and were grown ~16 h at 37 °C with shaking at 200 rpm. The following day, bacterial cultures were diluted in fresh prewarmed TCS (1:50 or 1:100 v/v), and cultured until an optical density (OD, measured at 600 nm) of 0.6.

Cloning. Primers used in this study were designed using NEBuilder Assembly Tool (https://nebuilder.neb.com/#!/). To produce *S. flexneri* expressing AfaI and GFP, the pACAfaI

plasmid was constructed (plasmids characteristics and primer sequences are located in **Supplementary Table 1**). Briefly, the *afaI* operon together with the amp^R gene was amplified from *S.flexneri afaI* strain using the primers *afaI-operon-fw* and *afaI-operon-rv*. The *ori p15A* was amplified from pAC-P_{lac} using the primers *p15A-ori-fw* and *p15A-ori-fw*. Both DNA fragments were assembled using the Gibson assembly to generate the plasmid pAC-AfaI-AmpR. In a second step, the *AmpR* gene from pAC-AfaI-Amp was substituted by the *CmR* gene and generate pAC-AfaI-Cm. This was achieved by amplification of the *CmR* gene from pNeae2 using the primers *CmR-fw CmR-rv* and amplification of the backbone of pAC-AfaI-Amp with primers *afaI-p15A-fw, afaI-p15A-rv*, followed by Gibson assembly. Gibson assembly was performed at 50 °C for 30 min using the HiFi DNA Assembly Master Mix (#E2621L, New England Biolabs). Resulting plasmid pAC-AfaI-Cm was transformed into *S. flexneri* GFP by electroporation.

Cell lines. HeLa (ATCC CCL-2) cells were grown at 37 °C and 5% CO_2 in Dulbecco's modified Eagle medium (DMEM, GIBCO) supplemented with 10% fetal bovine serum (FBS, Sigma-Aldrich). Cells lines were tested for mycoplasma infection and tested negative.

Infection of human cells. Hela cells were seeded in 96-well microplates (PhenoPlates, Perkin Elmer) at a confluency of 10^4 cells/well 2 days prior to infection. Alternatively, 9×10^4 HeLa cells were seeded in 6-well plates (Thermo Scientific) containing 22 × 22 mm glass coverslips 2 days before the infection. Bacterial cultures were grown as described and cell cultures were infected with *S. flexneri* strains as described previously (Mostowy et al., 2010). Briefly, Hela cells were infected with *S. flexneri* by spin-inoculation at 110 g for 10 min at a multiplicity of infection (MOI, bacteria:cell) of 100:1. Then, microplates were placed at 37 °C and 5% CO_2 for 30 min. Infected cultures were washed 3 × with phosphate-buffered saline (PBS) pH 7.4 and incubated with fresh DMEM containing 10% FBS and 50 mg/mL gentamicin at 37 °C and 5% CO_2 for 3 or 4 h. In order to obtain more instances of *S. flexneri* associated to SEPT7 in Figure

4H, one of the datasets was obtained after infection with *S. flexneri* expressing the adhesin AfaI (Labigne-Roussel & Falkow, 1988) and GFP to increase host cell invasion at a MOI of 10 in the absence of spin inoculation.

Click chemistry. To label *de novo* DNA and protein synthesis, Click-iT™ EdU Cell Proliferation Kit for Imaging (#C10337 Thermofisher Scientific) and Click-iT™ AHA Protein Synthesis HCS Assay (#C10289 Thermofisher Scientific) were used, respectively, according to the manufacturer instructions. In the case of AHA, cells were cultured in glutamine, cystine and methionine-free DMEM (#21013024 Thermofisher Scientific) for 1 h prior to the treatment. 10μM EdU and 25μM AHA were supplemented to live bacterial or mammalian cell cultures for 1h. Cells were fixed for immunofluorescence as indicated below. Click azide/alkyne reactions were performed after permeabilization and prior to antibody staining as indicated below, according to the manufacturer's instructions.

Immunofluorescence and fluorescence microscopy. Bacteria, coverslips or 96-well microplates containing adherent infected or uninfected cells were washed three times with PBS pH 7.4 and fixed 15 min in 4% paraformaldehyde (in PBS) at RT. Fixed cells were washed three times with PBS pH 7.4 and subsequently permeabilized 5min with 0.1% Triton X-100 (in PBS). Cells were then washed three times in PBS and incubated 1h with primary antibodies diluted in PBS supplemented with 0.1% Triton X-100 and 1% bovine serum albumin. Cells were then washed three times in PBS and incubated 45 min with anti-rabbit secondary antibodies diluted 0.1% Triton X-100 (in PBS), and Hoestch and Alexa-conjugated phalloidin where indicated. 96-well microplates were washed three times in PBS and preserved in 0.01% sodium azide (#10338380 Thermo Scientific) in PBS pH 7.4. Stained bacteria cultures and coverslips were washed three times with PBS pH 7.4 mounted on glass slides with ProLong™ Diamond Antifade Mountant (#P36970I Invitrogen). Fluorescence microscopy on stained bacteria was performed using a using a 63×/1.4 C-Plan Apo oil immersion lens on a Zeiss LSM

880 confocal microscope driven by ZEN Blacksoftware (v2.3). Microscopy images were obtained using z-stack image series taking 8–16 slices. Fluorescence microscopy on infected or uninfected cells was performed using a ZEISS Plan-APOCHROMAT 20× / 0.95 Autocorr Objective or a ZEISS Plan-APOCHROMAT 50×/1.2 water immersion lens coupled to a 0.5x tubelens on a Zeiss CellDiscoverer 7 with Airyscan detectors driven by ZEN Blue software (v3.5). Microscopy images were obtained using z-stack image series taking 32 slices. Confocal images were processed using Airyscan processing (Weinerfilter) using "Auto Filter" and "3D Processing" options.

Flow cytometry. 5 x 10^4 individual bacterial cells were analysed using flow cytometry with an LSRII flow cytometer (BD Biosciences). The data was analysed using FlowJo software, version 10.7.1. The median fluorescence of the bacterial population was determined and plotted for each staining.

Analysis pipelines. Number of bacteria per cell, as well as fluorescence of bacteria, nuclei and mammalian cells was analysed using CellProfiler (v.4.0.7) (Carpenter et al., 2006). Custom made segmentation and deep learning pipelines for the classification of septin cages were written in ImageJ and Python using Keras.

Statistics. All graphs were plotted and statistical analysis were performed using Prism. n.s: non-significant, *: p-value < 0.05, **: p-value < 0.01, ***: p-value < 0.001).

Code availability

Custom ImageJ macros, phyton scripts and Jupyter notebooks were annotated and deposited in Github (https://github.com/ATLopezJimenez/Toolset-high-content-analysis-of-Shigella-infection).

Acknowledgements

We thank members of the Mostowy and Brian Ho labs for helpful discussion. We thank François-Xavier Campbell-Valois for providing TSAR plasmids. We thank the instructors of

the EMBL course Deep Learning for Image Analysis, in particular Prof. Pejman Rasti. A.T.L.J. was funded by the Swiss National Science Foundation Early Postdoc.Mobility Fellowship (P2GEP3_188277) and the European Union's Horizon 2020 research and innovation program under the Marie Skłodowska - Curie grant agreement no. H2020-MSCA-IF- 2020-895330. D.B. was supported by the Deutsche Forschungsgemeinschaft (DFG) Walter Benjamin Programme (BR 6637/1-1). G.Ö.G. was funded by the Human Frontier Science Program (LT000436/2021-L). This research in S. Mostowy laboratory was supported by a Wellcome Trust Senior Research Fellowship (206444/Z/17/Z) and European Research Council Consolidator Grant (772853 - ENTRAPMENT).

Supplementary table S1.

Bacterial strain	**Genotype**	**Reference**
Shigella flexneri srv. 5a str. M90T	SmR	(Mostowy et al., 2010)
S. flexneri mCherry	Constitutively producing mCherry, $Carb^R$, Sm^R	(Mostowy et al., 2013)
S. flexneri afaI	Constitutively producing the adhesin AfaE, Amp^R, Sm^R	(Mostowy et al., 2010)
S. flexneri GFP	Constitutively producing GFP, $Carb^R$	(Mostowy et al., 2010)
S. flexneri GFP *afaI*	Constitutively producing the adhesin AfaE and GFP, Amp^R Cm^R, Sm^R	This study
Plasmid	**Characteristics**	**Reference**
pTSAR1ud2.4s	T3SS reporter	(Campbell-Valois et al., 2014)
pAC-P_{lac}	pACYC184 derived plasmid.	(Lobato-Márquez et al., 2015)
pAC-AfaI-AmpR	For constitutive expression of the adhesin AfaE, ori p15A, Amp^R	This study
pAC-AfaI-CmR	For constitutive expression of the adhesin AfaE, ori p15A, Cm^R	This study
Primer	**Sequence (5'-3')**	**Reference**
afaI-operon-fw	tgcgttgcgcgaagatcctttgatcttttctacgggg	This study
afaI-operon-rv	ggaagctaaacgagcccgatcttcccca	This study
p15A-ori-fw	atcgggctcgtttagcttccttagctcc	This study
p15A-ori-rv	aaggatcttcgcgcaacgcaattaatgtaag	This study
afaI-p15A-fw	cggggcgtaactgtcagaccaagtttac	This study
afaI-p15A-rv	ttttctccatactcttccttttcaatattattg	This study
CmR-fw	aaggaagagtatggagaaaaaaatcactggatataccaccgttgatatatccc	This study
CmR-rv	ggtctgacagttacgccccgccctgcca	This study

References

Ackermann, M. (2015). A functional perspective on phenotypic heterogeneity in microorganisms. Nature Reviews Microbiology, 13(8):497-50813. https://doi.org/10.1038/nrmicro3491

Avraham, R., Haseley, N., Brown, D., Penaranda, C., Jijon, H. B., Trombetta, J. J., Satija, R., Shalek, A. K., Xavier, R. J., Regev, A., & Hung, D. T. (2015). Pathogen Cell-to-Cell Variability Drives Heterogeneity in Host Immune Responses. Cell, 162(6), 1309–1321. https://doi.org/10.1016/J.CELL.2015.08.027

Aylan, B., Botella, L., Gutierrez, M. G., & Santucci, P. (2023). High content quantitative imaging of *Mycobacterium tuberculosis* responses to acidic microenvironments within human macrophages. FEBS Open Bio, 13(7), 1204–1217. https://doi.org/10.1002/2211-5463.13537

Berg, S., Kutra, D., Kroeger, T., Straehle, C. N., Kausler, B. X., Haubold, C., Schiegg, M., Ales, J., Beier, T., Rudy, M., Eren, K., Cervantes, J. I., Xu, B., Beuttenmueller, F., Wolny, A., Zhang, C., Koethe, U., Hamprecht, F. A., & Kreshuk, A. (2019). ilastik: interactive machine learning for (bio)image analysis. Nature Methods 16:12, 16(12), 1226–1232. https://doi.org/10.1038/s41592-019-0582-9

Bergounioux, J., Elisee, R., Prunier, A. L., Donnadieu, F., Sperandio, B., Sansonetti, P., & Arbibe, L. (2012). Calpain Activation by the *Shigella flexneri* Effector VirA Regulates Key Steps in the Formation and Life of the Bacterium's Epithelial Niche. Cell Host & Microbe, 11(3), 240–252. https://doi.org/10.1016/J.CHOM.2012.01.013

Bernardini, M. L., Mounier, J., D'Hauteville, H., Coquis-Rondon, M., & Sansonetti, P. J. (1989). Identification of icsA, a plasmid locus of *Shigella flexneri* that governs bacterial intra- and intercellular spread through interaction with F-actin. Proceedings of the

National Academy of Sciences of the United States of America, 86(10), 3867–3871. https://doi.org/10.1073/PNAS.86.10.3867

Boddy, K. C., Gao, A. D., Truong, D., Kim, M. S., Froese, C. D., Trimble, W. S., & Brumell, J. H. (2018). Septin-regulated actin dynamics promote *Salmonella* invasion of host cells. Cellular Microbiology, 20(10), e12866. https://doi.org/10.1111/CMI.12866

Brodin, P., & Christophe, T. (2011). High-content screening in infectious diseases. Current Opinion in Chemical Biology, 15(4), 534–539. https://doi.org/10.1016/J.CBPA.2011.05.023

Campbell-Valois, F. X., Schnupf, P., Nigro, G., Sachse, M., Sansonetti, P. J., & Parsot, C. (2014). A Fluorescent Reporter Reveals On/Off Regulation of the *Shigella* Type III Secretion Apparatus during Entry and Cell-to-Cell Spread. Cell Host & Microbe, 15(2), 177–189. https://doi.org/10.1016/J.CHOM.2014.01.005

Carpenter, A. E., Jones, T. R., Lamprecht, M. R., Clarke, C., Kang, I. H., Friman, O., Guertin, D. A., Chang, J. H., Lindquist, R. A., Moffat, J., Golland, P., & Sabatini, D. M. (2006). CellProfiler: Image analysis software for identifying and quantifying cell phenotypes. Genome Biology, 7(10), 1–11. https://doi.org/10.1186/GB-2006-7-10-R100

Davidson, M. S., Andradi-Brown, C., Yahiya, S., Chmielewski, J., O'Donnell, A. J., Gurung, P., Jeninga, M. D., Prommana, P., Andrew, D. W., Petter, M., Uthaipibull, C., Boyle, M. J., Ashdown, G. W., Dvorin, J. D., Reece, S. E., Wilson, D. W., Cunningham, K. A., Ando, D. Michael., Dimon, M., & Baum, J. (2021). Automated detection and staging of malaria parasites from cytological smears using convolutional neural networks. Biological Imaging, 1:e2. https://doi.org/10.1017/S2633903X21000015

Day, N. J., Santucci, P., & Gutierrez, M. G. (2023). Host cell environments and antibiotic efficacy in tuberculosis. Trends in Microbiology, 32(3):270-279. https://doi.org/10.1016/J.TIM.2023.08.009

Deboosere, N., Belhaouane, I., Machelart, A., Hoffmann, E., Vandeputte, A., & Brodin, P. (2021). High-Content Analysis Monitoring Intracellular Trafficking and Replication of *Mycobacterium tuberculosis* Inside Host Cells. Methods in Molecular Biology, 2314, 649–702. https://doi.org/10.1007/978-1-0716-1460-0_29

Dramé, M., Garcia-Rodriguez, F. J., Buchrieser, C., & Escoll, P. (2023). High-content assay to measure mitochondrial function and bacterial vacuole size in infected human primary macrophages. STAR Protocols, 4(2), 102175. https://doi.org/10.1016/J.XPRO.2023.102175

Egile, C., Loisel, T. P., Laurent, V., Li, R., Pantaloni, D., Sansonetti, P. J., & Carlier, M. F. (1999). Activation of the Cdc42 effector N-Wasp by the *Shigella flexneri* Icsa protein promotes actin nucleation by Arp2/3 complex and bacterial actin-based motility. Journal of Cell Biology, 146(6), 1319–1332. https://doi.org/10.1083/JCB.146.6.1319

Eliceiri, K. W., Berthold, M. R., Goldberg, I. G., Ibáñez, L., Manjunath, B. S., Martone, M. E., Murphy, R. F., Peng, H., Plant, A. L., Roysam, B., Stuurmann, N., Swedlow, J. R., Tomancak, P., & Carpenter, A. E. (2012). Biological imaging software tools. Nature Methods 9:7, 9(7), 697–710. https://doi.org/10.1038/nmeth.2084

Ennis, H. L., & Lubin, M. (1964). Cycloheximide: Aspects of inhibition of protein synthesis in mammalian cells. Science, 146(3650), 1474–1476. https://doi.org/10.1126/SCIENCE.146.3650.1474

Ezekiel, D. H., & Hutchins, J. E. (1968). Mutations affecting RNA Polymerase associated with Rifampicin Resistance in *Escherichia col*i. Nature, 220:5164, 220(5164), 276–277. https://doi.org/10.1038/220276a0

Fisch, D., Evans, R., Clough, B., Byrne, S. K., Channell, W. M., Dockterman, J., & Frickel, E. M. (2021). HRMAn 2.0: Next-generation artificial intelligence–driven analysis for broad

host–pathogen interactions. Cellular Microbiology, 23(7), e13349. https://doi.org/10.1111/CMI.13349

Fisch, D., Yakimovich, A., Clough, B., Wright, J., Bunyan, M., Howell, M., Mercer, J., & Frickel, E. (2019a). Defining host–pathogen interactions employing an artificial intelligence workflow. ELife, 12:8:e40560. https://doi.org/10.7554/ELIFE.40560

Global Burden of Disease Collaborative Network. (2020). Global Burden of Disease Study 2019 (GBD 2019). Institute for Health Metrics and Evaluation (IHME).

Gutierrez, M. G., & Enninga, J. (2022). Intracellular niche switching as host subversion strategy of bacterial pathogens. Current Opinion in Cell Biology, 76:102081. https://doi.org/10.1016/J.CEB.2022.102081

Hung, J., Goodman, A., Ravel, D., Lopes, S. C. P., Rangel, G. W., Nery, O. A., Malleret, B., Nosten, F., Lacerda, M. V. G., Ferreira, M. U., Rénia, L., Duraisingh, M. T., Costa, F. T. M., Marti, M., & Carpenter, A. E. (2020). Keras R-CNN: Library for cell detection in biological images using deep neural networks. BMC Bioinformatics, 21(1), 1–7. https://doi.org/10.1186/S12859-020-03635-X

Iwai, H., Kim, M., Yoshikawa, Y., Ashida, H., Ogawa, M., Fujita, Y., Muller, D., Kirikae, T., Jackson, P. K., Kotani, S., & Sasakawa, C. (2007). A Bacterial Effector Targets Mad2L2, an APC Inhibitor, to Modulate Host Cell Cycling. Cell, 130(4), 611–623. https://doi.org/10.1016/J.CELL.2007.06.043

Krizhevsky, A., Sutskever, I., & Hinton, G. E. (2012). ImageNet classification with deep convolutional neural networks. In Proceedings of the 26th International Conference on Neural Information Processing Systems - Volume 1 (NIPS'12), Vol. 1. Curran Associates Inc., Red Hook, NY, USA, 1097–1105.

Krokowski, S., Lobato-Márquez, D., Chastanet, A., Pereira, P. M., Angelis, D., Galea, D., Larrouy-Maumus, G., Henriques, R., Spiliotis, E. T., Carballido-López, R., & Mostowy,

S. (2018). Septins recognize and entrap dividing bacterial cells for delivery to lysosomes. Cell Host & Microbe, 24(6), 866-874.e4. https://doi.org/10.1016/j.chom.2018.11.005

Labigne-Roussel, A., & Falkow, S. (1988). Distribution and degree of heterogeneity of the afimbrial-adhesin-encoding operon (afa) among uropathogenic *Escherichia coli* isolates. Infection and Immunity, 56(3), 640–648. https://doi.org/10.1128/iai.56.3.640-648.1988

Lecun, Y., Bengio, Y., & Hinton, G. (2015). Deep learning. Nature 521, 436–444. https://doi.org/10.1038/nature14539

Lensen, A., Gomes, M. C., López-Jiménez, A. T., & Mostowy, S. (2023). An automated microscopy workflow to study Shigella–neutrophil interactions and antibiotic efficacy in vivo. DMM Disease Models and Mechanisms, 16(6). https://doi.org/10.1242/dmm.049908

Lobato-Márquez, D., Conesa, J. J., López-Jiménez, A. T., Divine, M. E., Pruneda, J. N., & Mostowy, S. (2023). Septins and K63 ubiquitin chains are present in separate bacterial microdomains during autophagy of entrapped *Shigella*. Journal of Cell Science, 136(7). https://doi.org/10.1242/JCS.261139

Lobato-Márquez, D., Moreno-Córdoba, I., Figueroa, V., Diáz-Orejas, R., & Garciá-Del Portillo, F. (2015). Distinct type I and type II toxin-antitoxin modules control *Salmonella* lifestyle inside eukaryotic cells. Scientific Reports 20:5:9374. https://doi.org/10.1038/srep09374

Lobato-Márquez, D., Xu, J., Güler, G. Ö., Ojiakor, A., Pilhofer, M., & Mostowy, S. (2021). Mechanistic insight into bacterial entrapment by septin cage reconstitution. Nature Communications 12(1):4511. https://doi.org/10.1038/s41467-021-24721-5

Martins, C. S., Taveneau, C., Castro-Linares, G., Baibakov, M., Buzhinsky, N., Eroles, M., Milanović, V., Omi, S., Pedelacq, J.-D., Iv, F., Bouillard, L., Llewellyn, A., Gomes, M., Belhabib, M., Kuzmić, M., Verdier-Pinard, P., Lee, S., Badache, A., Kumar, S., …

Mavrakis, M. (2023). Human septins organize as octamer-based filaments and mediate actin-membrane anchoring in cells. Journal of Cell Biology, 222(3). https://doi.org/10.1083/JCB.202203016/213778

Mattiazzi Usaj, M., Styles, E. B., Verster, A. J., Friesen, H., Boone, C., & Andrews, B. J. (2016). High-Content Screening for Quantitative Cell Biology. Trends in Cell Biology, 26(8), 598–611. https://doi.org/10.1016/J.TCB.2016.03.008

McDonald, P. C., & Dedhar, S. (2024). Persister cell plasticity in tumour drug resistance. Seminars in Cell & Developmental Biology, 156, 1–10. https://doi.org/10.1016/J.SEMCDB.2023.11.003

Mostowy, S., Bonazzi, M., Hamon, M. A., Tham, T. N., Mallet, A., Lelek, M., Gouin, E., Demangel, C., Brosch, R., Zimmer, C., Sartori, A., Kinoshita, M., Lecuit, M., & Cossart, P. (2010). Entrapment of intracytosolic bacteria by septin cage-like structures. Cell Host & Microbe, 8(5), 433–444. https://doi.org/10.1016/J.CHOM.2010.10.009

Mostowy, S., Boucontet, L., Mazon Moya, M. J., Sirianni, A., Boudinot, P., Hollinshead, M., Cossart, P., Herbomel, P., Levraud, J.-P. P., & Colucci-Guyon, E. (2013). The zebrafish as a new model for the in vivo study of *Shigella flexneri* interaction with phagocytes and bacterial autophagy. PLoS Pathogens, 9(9), e1003588. https://doi.org/10.1371/journal.ppat.1003588

Mostowy, S., & Cossart, P. (2012). Septins: the fourth component of the cytoskeleton. Nature Reviews Molecular Cell Biology, 13(3), 183–194. https://doi.org/10.1038/nrm3284

Mostowy, S., Nam Tham, T., Danckaert, A., Guadagnini, S., Boisson-Dupuis, S., Pizarro-Cerdá, J., & Cossart, P. (2009). Septins Regulate Bacterial Entry into Host Cells. PLoS ONE, 4(1), e4196. https://doi.org/10.1371/journal.pone.0004196

Nielsen, M. A. (2015). Neural Networks and Deep Learning. Determination press.

Ortega, F. E., Koslover, E. F., & Theriot, J. A. (2019). *Listeria monocytogenes* cell-to-cell spread in epithelia is heterogeneous and dominated by rare pioneer bacteria. ELife, 8. https://doi.org/10.7554/ELIFE.40032

Parsot, C., Ménard, R., Gounon, P., & Sansonetti, P. J. (1995). Enhanced secretion through the *Shigella flexneri* Mxi□Spa translocon leads to assembly of extracellular proteins into macromolecular structures. Molecular Microbiology, 16(2), 291–300. https://doi.org/10.1111/J.1365-2958.1995.TB02301.X

Pedrali-Noy, G., Spadari, S., Miller-Faurès, A., Miller, A. O. A., Kruppa, J., & Koch, G. (1980). Synchronization of HeLa cell cultures by inhibition of DNA polymerase alpha with aphidicolin. Nucleic Acids Research, 8(2), 377. https://doi.org/10.1093/NAR/8.2.377

Pegoraro, G., & Misteli, T. (2017). High-Throughput Imaging for the Discovery of Cellular Mechanisms of Disease. Trends in Genetics, 33(9), 604–615. https://doi.org/10.1016/J.TIG.2017.06.005

Pylkkö, T., Ilina, P., & Tammela, P. (2021). Development and validation of a high-content screening assay for inhibitors of enteropathogenic *E. coli* adhesion. Journal of Microbiological Methods, 184, 106201. https://doi.org/10.1016/J.MIMET.2021.106201

Ray, K., Bobard, A., Danckaert, A., Paz-Haftel, I., Clair, C., Ehsani, S., Tang, C., Sansonetti, P., Van Nhieu, G. T., & Enninga, J. (2010). Tracking the dynamic interplay between bacterial and host factors during pathogen-induced vacuole rupture in real time. Cellular Microbiology, 12(4), 545–556. https://doi.org/10.1111/J.1462-5822.2010.01428.X

Robertin, S., Brokatzky, D., Lobato-Márquez, D., & Mostowy, S. (2023). Regulation of integrin α5β1-mediated *Staphylococcus aureus* cellular invasion by the septin cytoskeleton. European Journal of Cell Biology, 102(4), 151359. https://doi.org/10.1016/J.EJCB.2023.151359

Robertin, S., & Mostowy, S. (2020). The history of septin biology and bacterial infection. Cellular Microbiology, 22(4), e13173. https://doi.org/10.1111/CMI.13173

Santucci, P., Greenwood, D. J., Fearns, A., Chen, K., Jiang, H., & Gutierrez, M. G. (2021). Intracellular localisation of *Mycobacterium tuberculosis* affects efficacy of the antibiotic pyrazinamide. Nature Communications 12(1):3816 https://doi.org/10.1038/s41467-021-24127-3

Schnupf, P., & Sansonetti, P. J. (2019). Shigella Pathogenesis: New Insights through Advanced Methodologies. Microbiology Spectrum 7(2):10.1128. https://doi.org/10.1128/microbiolspec.bai-0023-2019

Snijder, B., Sacher, R., Rämö, P., Damm, E. M., Liberali, P., & Pelkmans, L. (2009). Population context determines cell-to-cell variability in endocytosis and virus infection. Nature, 461(7263):520-3. https://doi.org/10.1038/nature08282

Soroor, F., Kim, M. S., Palander, O., Balachandran, Y., Collins, R. F., Benlekbir, S., Rubinstein, J. L., & Trimble, W. S. (2021). Revised subunit order of mammalian septin complexes explains their in vitro polymerization properties. Molecular Biology of the Cell, 32(3):289-300. https://doi.org/10.1091/MBC.E20-06-0398

Spiliotis, E. T., & Nakos, K. (2021). Cellular functions of actin- and microtubule-associated septins. Current Biology, 31(10):R651-R666. https://doi.org/10.1016/J.CUB.2021.03.064

Stringer, C., Wang, T., Michaelos, M., & Pachitariu, M. (2020). Cellpose: a generalist algorithm for cellular segmentation. Nature Methods 8(1):100-106. https://doi.org/10.1038/s41592-020-01018-x

Sugino, A., Peebles, C. L., Kreuzer, K. N., & Cozzarelli, N. R. (1977). Mechanism of action of nalidixic acid: Purification of *Escherichia coli* nalA gene product and its relationship to DNA gyrase and a novel nicking-closing enzyme. Proceedings of the National Academy of Sciences, 74(11), 4767–4771. https://doi.org/10.1073/PNAS.74.11.4767

Szuba, A., Bano, F., Castro-Linares, G., Iv, F., Mavrakis, M., Richter, R. P., Bertin, A., & Koenderink, G. H. (2021). Membrane binding controls ordered self-assembly of animal septins. ELife, 10:e63349. https://doi.org/10.7554/ELIFE.63349

Toniolo, C., Rutschmann, O., & McKinney, J. D. (2021). Do chance encounters between heterogeneous cells shape the outcome of tuberculosis infections? Current Opinion in Microbiology, 59, 72–78. https://doi.org/10.1016/J.MIB.2020.08.008

Touquet, B., Pelissier, L., Cavailles, P., Yi, W., Bellini, V., Mercier, C., Cesbron-Delauw, M. F., Boumendjel, A., & Aldebert, D. (2018). High-content imaging assay to evaluate *Toxoplasma gondii* infection and proliferation: A multiparametric assay to screen new compounds. PLOS ONE, 13(8), e0201678. https://doi.org/10.1371/JOURNAL.PONE.0201678

van Tartwijk, F. W., & Kaminski, C. F. (2022). Protein Condensation, Cellular Organization, and Spatiotemporal Regulation of Cytoplasmic Properties. Advanced Biology, 6(11):e2101328. https://doi.org/10.1002/ADBI.202101328

von Chamier, L., Laine, R. F., Jukkala, J., Spahn, C., Krentzel, D., Nehme, E., Lerche, M., Hernández-Pérez, S., Mattila, P. K., Karinou, E., Holden, S., Solak, A. C., Krull, A., Buchholz, T. O., Jones, M. L., Royer, L. A., Leterrier, C., Shechtman, Y., Jug, F., … Henriques, R. (2021). Democratising deep learning for microscopy with ZeroCostDL4Mic. Nature Communications 12(1):2276. https://doi.org/10.1038/s41467-021-22518-0

Voznica, J., Gardell, C., Belotserkovsky, I., Dufour, A., Enninga, J., & Stévenin, V. (2018). Identification of parameters of host cell vulnerability during *Salmonella* infection by quantitative image analysis and modeling. Infection and Immunity, 86(1):e00644-17. https://doi.org/10.1128/IAI.00644-17/

Wang, X., Pernicone, N., Pertz, L., Hua, D., Zhang, T., Listovsky, T., & Xie, W. (2019). REV7 has a dynamic adaptor region to accommodate small GTPase RAN/*Shigella* IpaB ligands, and its activity is regulated by the RanGTP/GDP switch. Journal of Biological Chemistry, 294(43), 15733–15742. https://doi.org/10.1074/JBC.RA119.010123

Weigert, M., Schmidt, U., Haase, R., Sugawara, K., & Myers, G. (2020, March). Star-convex Polyhedra for 3D Object Detection and Segmentation in Microscopy. 2020 IEEE Winter Conference on Applications of Computer Vision (WACV). https://doi.org/10.1109/WACV45572.2020.9093435

Woods, B. L., & Gladfelter, A. S. (2021). The state of the septin cytoskeleton from assembly to function. Current Opinion in Cell Biology, 68:105-112. https://doi.org/10.1016/J.CEB.2020.10.007

Zhang, Q., Xian, W., Li, Z., Lu, Q., Chen, X., Ge, J., Tang, Z., Liu, B., Chen, Z., Gao, X., Hottiger, M. O., Zhang, P., Qiu, J., Shao, F., & Liu, X. (2024). *Shigella* induces stress granule formation by ADP-riboxanation of the eIF3 complex. Cell Reports, 43(2):113789. https://doi.org/10.1016/J.CELREP.2024.113789

Figure legends.

Figure 1. High-content imaging captures the heterogeneity of *S. flexneri* infection. (A) Representative high-resolution microscopy image of HeLa cells infected with *S. flexneri* expressing mCherry acquired with the high-content microscope ZEISS CellDiscoverer7. Scale bar, 10 µm. (B) Enlarged view of insets in A, highlighting a *S. flexneri* bacteria polymerising an actin tail (1) and entrapped in a septin cage (2), scale bar, 1 µm. (C) Percentage of infected cells at 3 h.p.i. of 7 independent experiments. Graph represents mean = 11.49% ± SD = 4.36%. (D) Percentage of infected cells harbouring different bacterial doses, graph represents mean ± SD. (E) Distance of the bacteria to the centroid of the host cell. Graph represents the median (8.74 µm) and interquartile range (6.51 – 11.05 µm). Values from n = 4990 cells from 7 independent experiments. (F) Distance of individual bacteria to the centroid of the host cell depending on its bacterial load. Graph represents the median and interquartile range. Kruskal-Wallis test and Dunn's multiple comparisons test. (G) Area of cells depending on infection. Graph represents the median area (uninfected: 3031 μm^2, infected: 4148 μm^2) and interquartile range (unifected: 2308 – 4169 μm^2, infected: 3062 – 5752 μm^2). Values from n = 9469 uninfected cells and n = 1031 infected cells from 7 independent experiments. (H) Area of infected cells depending on its bacterial load. Graph represents the median and interquartile range. Kruskal-Wallis test and Dunn's multiple comparisons test. (I) Nuclear area of cells depending on infection. Graph represents the median area (uninfected: 1551 μm^2, infected: 1897 μm^2) and interquartile range (unifected: 1209 - 1950 μm^2, infected: 1486 - 2333 μm^2). Values from n = 9469 uninfected cells and n = 1031 infected cells from 7 independent experiments. (J) Nuclear area of infected cells depending on its bacterial load. Graph represents the median and interquartile range. Kruskal-Wallis test and Dunn's multiple comparisons test.

Figure 2: *S. flexneri* infection reduces host DNA synthesis and host protein synthesis. (A) Representative microscopy image of HeLa cells infected with *S. flexneri* expressing mCherry at 3 h.p.i, after 1h incubation with Click-IT Edu. Asterisks label the nucleus of infected cells with reduced Edu incorporation. Contour of selected cells is delimited with a dashed line. Scale bar, 10 µm. (B) Edu acquisition in uninfected cells is bimodal. Graph represents the normalised median of the ratio between the fluorescence intensity of Edu and Hoechst (1), and interquartile range (0.5924 – 31.22). Values from n = 8941 cells from 3 independent experiments. An arbitrary threshold of 5 is selected to define cells in S-phase. (C) Frequency of cells in S-phase (as defined in B) depending on infection. Graph represents mean ± SD (uninfected: 34.45% ± 9.78%, infected: 35.89% ± 4.69%). Student's t-test. (D) Edu acquisition in cells in S-phase depending on infection. Graph representes the normalised median of the ratio between the fluorescence intensity of Edu and Hoechst (uninfected: 75.14, infected: 44.73), and interquartile range (uninfected: 27.89 – 131.0, infected: 22.05 – 93.36), from 3065 uninfected and 552 infected cells. Mann-Whitney U test. (E) Edu acquisition in cells in S-phase depending on bacterial load. Graph represents the median and interquartile range. Kruskal-Wallis test and Dunn's multiple comparisons test. (F) Representative microscopy image of HeLa cells infected with *S. flexneri* expressing mCherry at 3 h.p.i, after 1h incubation with Click-IT AHA. Asterisks label the infected cells with reduced AHA incorporation. Scale bar, 10 µm. (G). AHA acquisition in host cells depending on infection. Graph representes the normalised median of AHA fluorescence intensity (uninfected: 1, infected: 0.86), and interquartile range (uninfected: 0.7850 – 2.694, infected: 0.6207 – 1.241), from 36 uninfected and 233 infected cells. Mann-Whitney U test. (H) AHA acquisition in infected cells depending on bacterial load. Graph represents the median and interquartile range. Kruskal-Wallis test and Dunn's multiple comparisons test.

Figure 3. Microscopy pipeline to automatically identify SEPT7-*S. flexneri* interactions. (A) Diagram representing the steps involved in the imaging and analysis pipeline. After infection, fixation and staining, high number of images are automatically acquired using the high-content microscope. Scale bar, 10 µm. These are then processed to segment bacteria based on their fluorescence, so that a square field containing the bacteria in the centre is cropped and saved for subsequent analysis. A deep learning model based on CNN is applied using Jupiter notebooks and the Python Keras library hosted on Colab to sort individual, isolated bacteria. Several processing steps are applied using Python to remove noise (band-pass filtering by difference of Gaussian and mean filters), normalise the data across datasets for comparison, and remove signal away from the bacteria which is irrelevant for the identification of SEPT7 assemblies. Scale bar, 1 µm. Finally, a similar second deep learning model based on CNN is applied to identify SEPT7 interacting with bacteria.

Figure 4. Training of a deep learning algorithm to identify single isolated bacteria cells and SEPT7 associated *S. flexneri*. (A) Table summarizing the annotated dataset used for the training process. The labels of the two classification classes used were “Single bacteria” and “Clump”. The annotated images were randomly split into two groups, one used as training dataset (comprising 80% of the images) and another used as validation dataset (with the remaining 20%). A separate annotated dataset was used for testing. (B) Representative Airyscan images of bacteria used for each class. 2D max projections of Z-stacks were used for training. Scale bar, 1 µm. (C) Architecture of the deep learning algorithm used for training. Each raw describes the characteristics of the sequential transformation steps applied. Conv2D stands for 2D Convolution. (D, E) Accuracy and Loss as metrics to represent the training process over subsequent epochs (entire passing of the training data through the algorithm). Accuracy increases and loss decreases for both training and validation datasets, indicating a

good fit of the model to the data. Vertical dashed grey line indicates Early Stopping, or epoch value for the minimum validation Loss. (F) Confusion matrix performed on an annotated test dataset not used previously for the training or validation process, indicating the percentage of predictions that were correct or wrong for each class. (G) Precision, recall and f1 score as metrics that summarize the performance of the model or classifier. (H) Table summarizing the annotated dataset used for the training process. The labels of the two classification classes used were “Septin” and “Negative”. The annotated images were randomly split into three groups, one used as training dataset (comprising 75% of the images), another used as validation dataset (with 15%) and a last one used as test dataset (with 10%). Due to the data being very imbalanced (15% natural frequency of SEPT7 associated bacteria), the images comprised in the Negative class were under-sampled as indicated in the table. (I) Representative Airyscan images of bacteria used for each class. 2D max projections of Z-stacks were used for training. Scale bar, 1 µm. (J) Architecture of the deep learning algorithm used for training. Each raw describes the characteristics of the sequential transformation steps applied. Conv2D stands for 2D Convolution, Batch_norm stands for Batch normalisation. (K, L) Accuracy and Loss as metrics to represent the training process over subsequent epochs. Accuracy increases and loss decreases for both training and validation datasets, indicating a good fit of the model to the data. Vertical dashed grey line indicates Early Stopping, or epoch value for the minimum validation Loss. (M) Confusion matrix performed on the test dataset not used previously for the training or validation process, indicating the percentage of predictions that were correct or wrong for each class. (N) Precision, recall and f1 score as metrics that summarize the performance of the model or classifier.

Figure 5. Septin assemblies associated to *S. flexneri* are heterogeneous. (A) Selected examples of the training dataset to showcase the diverse morphology of septin assemblies

associated to bacteria. Frequent morphologies include (a) ring like structures around the bacteria, (b) smooth tight recruitment around the entire bacterial surface, (c) loose structures more distant from the bacterial surface, (d) septin recruitment to both bacterial poles, (e) septin recruitment to a single bacterial pole. Scale bar, 1 µm. (B) Intensity profiles of the cytosolic bacterial mCherry and the SEPT7 recruitment, as indicated in the white and orange dashed lines, respectively. (C) Pie chart representing the relative frequency of 855 *S. flexneri*- SEPT7 associations depicted in A.

Figure 6. *S. flexneri* associated with SEPT7 are metabolically active. (A) Representative microscopy image of HeLa cells infected with *S. flexneri* expressing mCherry at 3 h.p.i, after 1h incubation with Click-IT Edu. Scale bar 10 µm. (B) Enlarged view of insets in A, highlighting a *S. flexneri* associated or not to SEPT7 structures. Scale bar, 1 µm. (C) Frequency of the number of SEPT7-associated bacteria identified using deep learning from experiments in A, from n= 1024 from 3 independent replicates. Graph represents mean ± SD (9.23% ± 2.62%). (D) Normalised ratio between Edu signal and mCherry in individual bacteria. Graph representes the median (negatives: 1, septin associated: 1.059), and interquartile range (negatives: 0.8185 – 1.207, septin associated: 0.8573 – 1.487). Mann-Whitney U test. (E) Representative microscopy image of HeLa cells infected with *S. flexneri* expressing mCherry at 3 h.p.i, after 1h incubation with Click-IT AHA. Scale bar 10 µm. (F) Enlarged view of insets in E, highlighting a *S. flexneri* associated or not to SEPT7 assemblies. Scale bar, 1 µm. (G) Frequency of the number of SEPT7-associated bacteria identified using deep learning from experiments in E, from n = 1872 bacteria from 3 independent replicates. Graph represents mean ± SD (7.01% ± 2.41%). (D) Normalised AHA signal in individual bacteria in A, B. Graph representes the median (negatives: 1, SEPT7 associated: 1.055), and interquartile range (negatives: 0.6986 – 1.345, SEPT7 associated: 0.7837 – 1.497). Mann-Whitney U test.

Figure 7. *S. flexneri* associated with SEPT7 have an active T3SS. (A) Representative microscopy image of HeLa cells infected with *S. flexneri* expressing the TSAR reporter at 3 h.p.i. Scale bar 10 µm. Arroheads highlight TSAR+ bacteria. Selected infected cells contours are delimited with dashed lines. (B) Distribution of TSAR signal intensity in individual bacteria. Graph represents the normalised median of the ratio between TSAR and mCherry (1), and interquartile range (0.7827 – 1.369). Values from n = 3654 bacterial cells from 3 independent experiments. An arbitrary threshold of 1.5 is selected to define TSAR+ *S. flexneri.* (C) Intensity of TSAR signal in individual bacteria depending on infection load of host cells. Graph represents the normalised median and interquartile range. Kruskal-Wallis test and Dunn's multiple comparisons test. (D) Representative microscopy image of HeLa cells infected with *S. flexneri* expressing the TSAR reporter at 3 h.p.i. Scale bar 10 µm. (E) Enlarged view of insets in D, highlighting a *S. flexneri* associated or not to SEPT7 assemblies. Scale bar, 1 µm. (F) Frequency of the number of SEPT7-associated bacteria identified using deep learning from experiments in F, from n= 5030 bacteria from 4 independent replicates. Graph represents mean ± SD (9.044% ± 5.582%). (G) Percentage of TSAR+ *S. flexneri* depending on their association to SEPT7. Graph represents mean ± SD (negatives: 2.214 ± 1.603, septin associated: 17.74 ± 5.138). Student's t-test. (H) Normalised ratio between TSAR signal and mCherry in individual bacteria. Graph representes the median (negatives: 1, SEPT7 associated: 1.122), and interquartile range (negatives: 0.7674 – 1.286, SEPT7 associated: 0.9047 – 1.511). Mann-Whitney U test.

Supplementary Figure Legends.

Figure 1-figure supplement 1. *S. flexneri* infection induces host cell size changes. (A) Representative images used as input for CellProfiler analysis (top), and their corresponding segmentations (bottom). Host cell boundaries were identified using a propagation method from the identified nucleus based on Otsu thresholding. (B) Hoestch fluorescence intensity of sum-projected nuclei as proxy of nuclear volume. Graph represents normalised median (uninfected: 1, infected: 1.294) and interquartile range (uninfected: 0.7588 – 1.287, infected: 0.9534 – 1.878) of n=2071 uninfected cells and n=195 infected cells from 3 independent experiments. Mann-Whitney U test. (C – D) Cell and nuclear area in presence and absence of infection and Latrunculin B. Graph represents the median and interquartile range. Kruskal-Wallis test and Dunn's multiple comparisons test.

Figure 2-figure supplement 1. Click-IT Edu and Click-IT AHA specifically label *de novo* DNA and protein synthesis in Hela cells. (A) Representative widefield image of HeLa cells after Click-IT Edu reaction in the presence or absence of Aphidicolin to inhibit eukaryotic DNA replication. Scale bar, 10 µm. (B) Quantification of *de novo* DNA synthesis in single HeLa cells in A as the ratio of nuclear Click-IT Edu signal to Hoechst. Graph represents the normalised median (untreated: 1, Aphidicolin: 0.7667) and interquartile range (untreated: 0.8474 – 6.571, Aphidicolin: 0.6816 – 0.8543) from 15828 untreated and 14943 treated cells from 3 independent experiments. Mann-Whitney U test. (C) Representative Airyscan confocal images of HeLa cells after Click-IT AHA reaction in the presence or absence of Cycloheximide to block eukaryotic translational elongation. Scale bar, 10 µm. (D) Quantification of cytoplasmic Click-IT AHA signal of the HeLa cells in A. Graph represents normalised median (untreated: 1, Cycloheximide: 0.3531) and interquartile range (untreated :0.6794 – 1.401,

Cycloheximide: 0.2504 – 0.6637) of n=268 untreated and n= 258 Cycloheximide treated cells from 3 independent experiments. Mann-Whitney U test.

Figure 4-figure supplement 1. Additional examples of the annotated datasets for deep learning. (A) Representative images of multiple bacteria associated to SEPT7. Scale bar, 1 µm. (B) Representative images of the training and validation dataset to identify single bacteria versus clumps. Scale bar, 5 µm. (C) Representative images of the training and validation dataset to identify SEPT7-positive versus SEPT7-negative bacteria, after processing. Scale bar, 5 µm.

Figure 5-figure supplement 1. Probability maps of SEPT7 around *S. flexneri.* (A, C) Median of the signal for mCherry and SEPT7 in both datasets (SEPT7-positive and SEPT7-negative), centered at the bacterial midbody or bacterial pole, respectively. Only bacteria with width ≥ 2.5 µm were selected to ensure bacteria were mostly transversal to the acquisition axis. Scale bar, 1 µm. (B,C) Quantification of SEPT7 signal and *S. flexneri* mCherry signal in the midbody projection depicted in A and transversal dash line indicated in B.

Figure 6-figure supplement 1. Click-IT Edu and Click-IT AHA specifically label *de novo* DNA and protein translation in *S. flexneri.* (A) Representative Airyscan image of mCherry *S. flexneri* after Click-IT Edu reaction in the presence or absence of Nalidixic acid to block bacterial DNA replication. Scale bar, 1 µm. (B) Quantification of Click-IT Edu signal of bacteria in C measured by FACS. Graph represents normalised mean ± SD. One-way ANOVA and Tukey's multiple comparisons test. (C) Representative Airyscan confocal images of HeLa cells infected with mCherry expressing *S. flexneri* after Click-IT Edu reaction in the presence or absence of Nalidixic acid to inhibit bacterial DNA nuclear replication. Scale bar, 10 µm. (D)

Quantification of *de novo* DNA synthesis in single bacteria in E as the ratio of nuclear Click-IT signal to Hoechst. Graph represents normalised median (untreated: 1, Nalidixic acid: 0.0646) and interquartile range (untreated: 0.3589 – 1.924, Nalidixic acid: 0.0350 – 0.3080) of 9310 untreated and 4368 Nalidixic acid treated bacteria from 3 independent experiments. Mann-Whitney U test. (E) Representative Airyscan confocal images of HeLa cells infected with mCherry expressing *S. flexneri* after Click-IT AHA reaction in the presence or absence of Rifampicin to block prokaryotic translation. Scale bar, 10 µm; insets, 1 µm. (F) Quantification of cytoplasmic Click-IT AHA signal of individual *S. flexneri* cells in C. Graph represents normalised median (untreated: 1, Rifampicin: 0.8263) and interquartile range (untreated: 0.7520 – 1.350, Rifampicin: 0.6143 – 1.100) of n=2309 untreated and n=345 Rifampicin treated bacteria from 3 independent experiments.

Figure 7-figure supplement 1. TSAR labels T3SS activity specifically. (A) Representative Airyscan confocal images of *S. flexneri* harbouring the TSAR plasmid grown in broth in the presence or absence of congo red to induce the expression of the T3SS. Scale bar, 1 µm. (B) Quantification of the TSAR dependent GFP signal of bacteria in A measured by FACS. Graph represents the normalised mean ± SD (untreated: 1 ± 0, congo red: 155.4 ± 125.2) from 4 independent experiments. (C) Representative examples of TSAR-positive *S. flexneri* associated to SEPT7. C stands for “cage”, P stands for “protrusion”. Scale bar 5 µm.

Figure 1

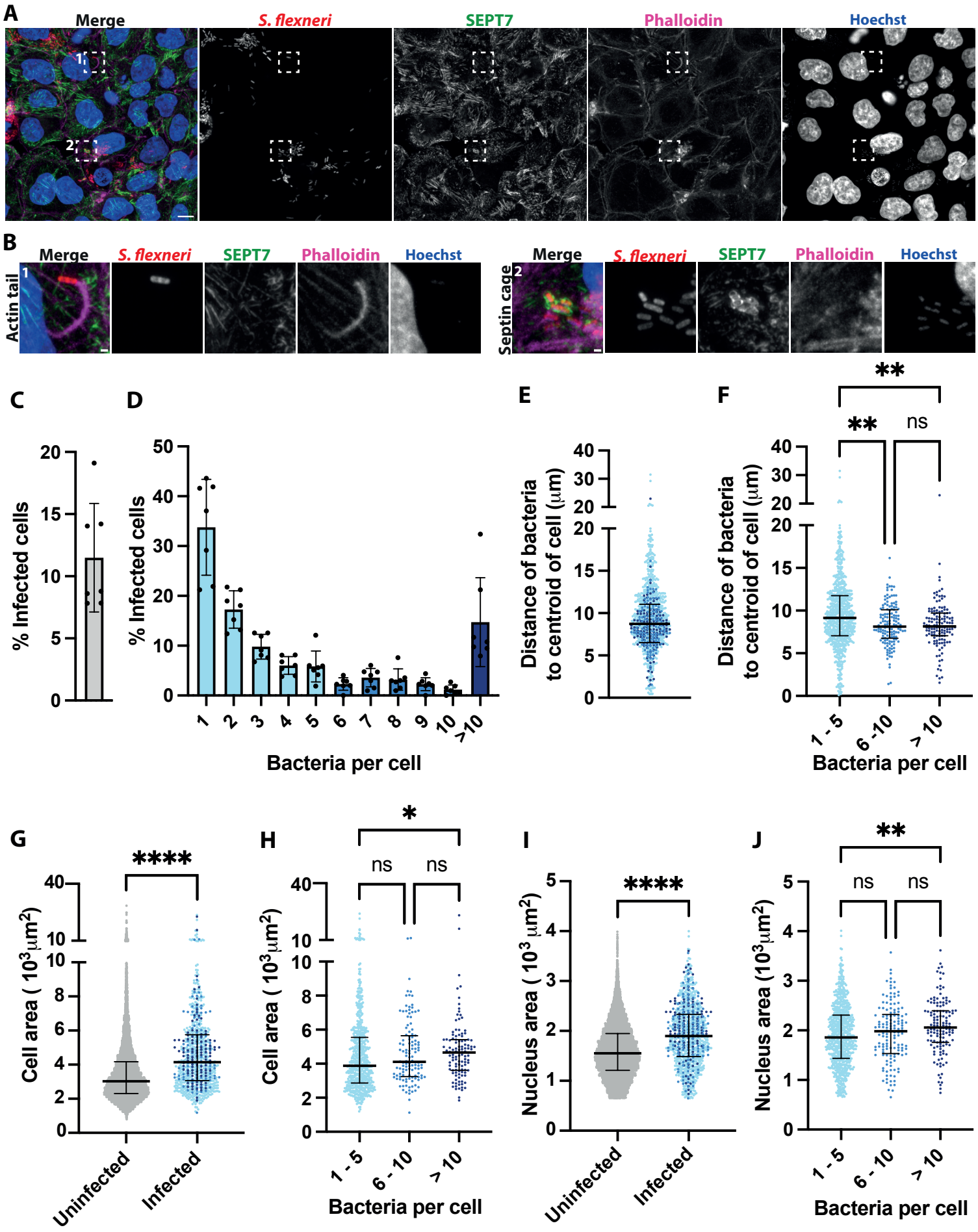
A
Merge
S. flexneri
SEPT7
Phalloidin
Hoechst
B
Actin tail
Septin cage
C
% Infected cells
D
% Infected cells
Bacteria per cell
E
Distance of bacteria to centroid of cell (μm)
F
Distance of bacteria to centroid of cell (μm)
Bacteria per cell
G
Cell area (10³μm²)
Uninfected
Infected
H
Cell area (10³μm²)
Bacteria per cell
I
Nucleus area (10³ μm²)
Uninfected
Infected
J
Nucleus area (10³μm²)
Bacteria per cell

Figure 2

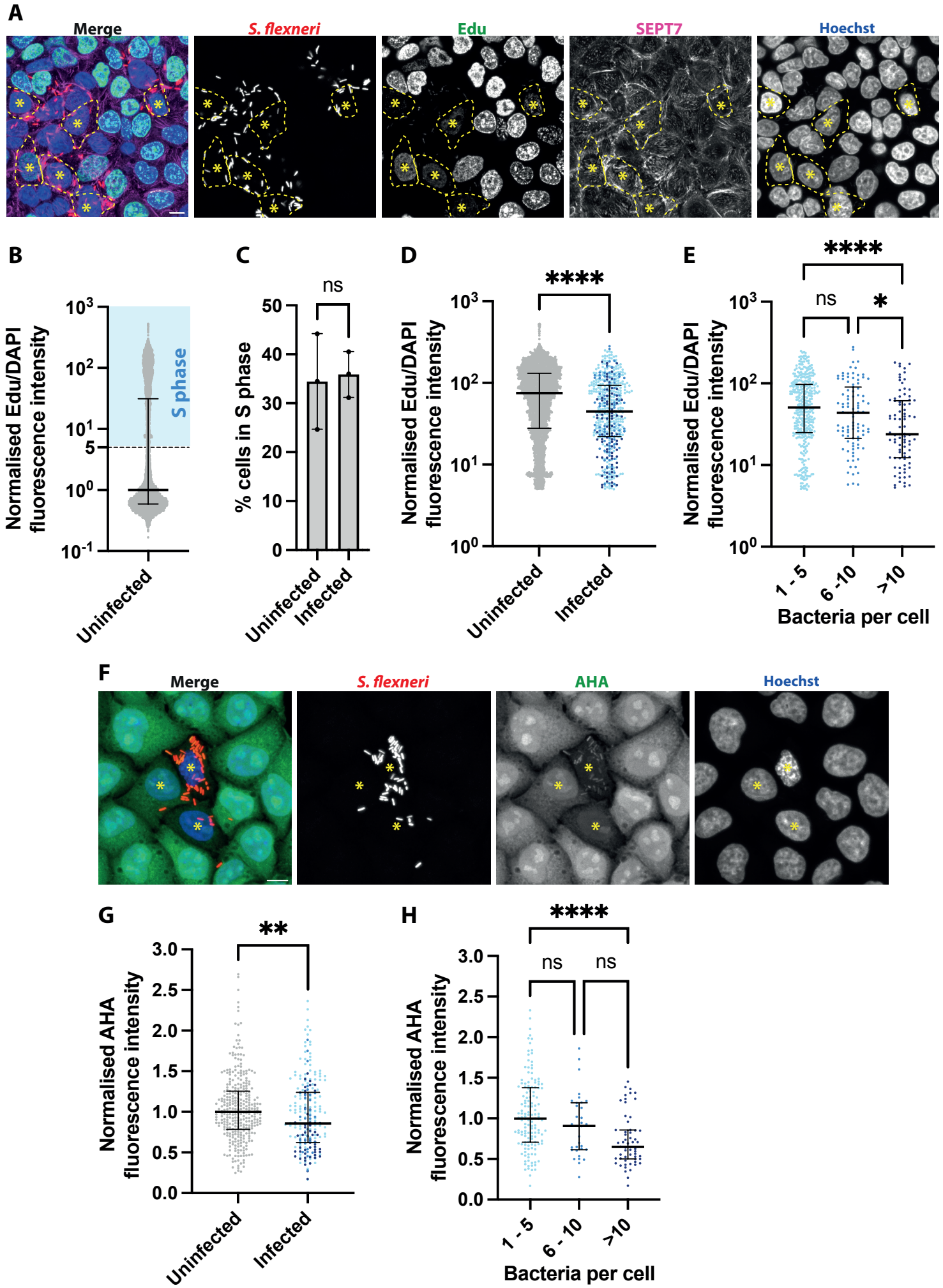
A
Merge
S. flexneri
Edu
SEPT7
Hoechst
B
Normalised Edu/DAPI fluorescence intensity
S phase
Uninfected
C
ns
% cells in S phase
Uninfected
Infected
D
****
Normalised Edu/DAPI fluorescence intensity
Uninfected
Infected
E
****
ns
*
Normalised Edu/DAPI fluorescence intensity
1 - 5
6 -10
>10
Bacteria per cell
F
Merge
S. flexneri
AHA
Hoechst
G
**
Normalised AHA fluorescence intensity
Uninfected
Infected
H
****
ns
ns
Normalised AHA fluorescence intensity
1 - 5
6 - 10
>10
Bacteria per cell

Figure 3

A

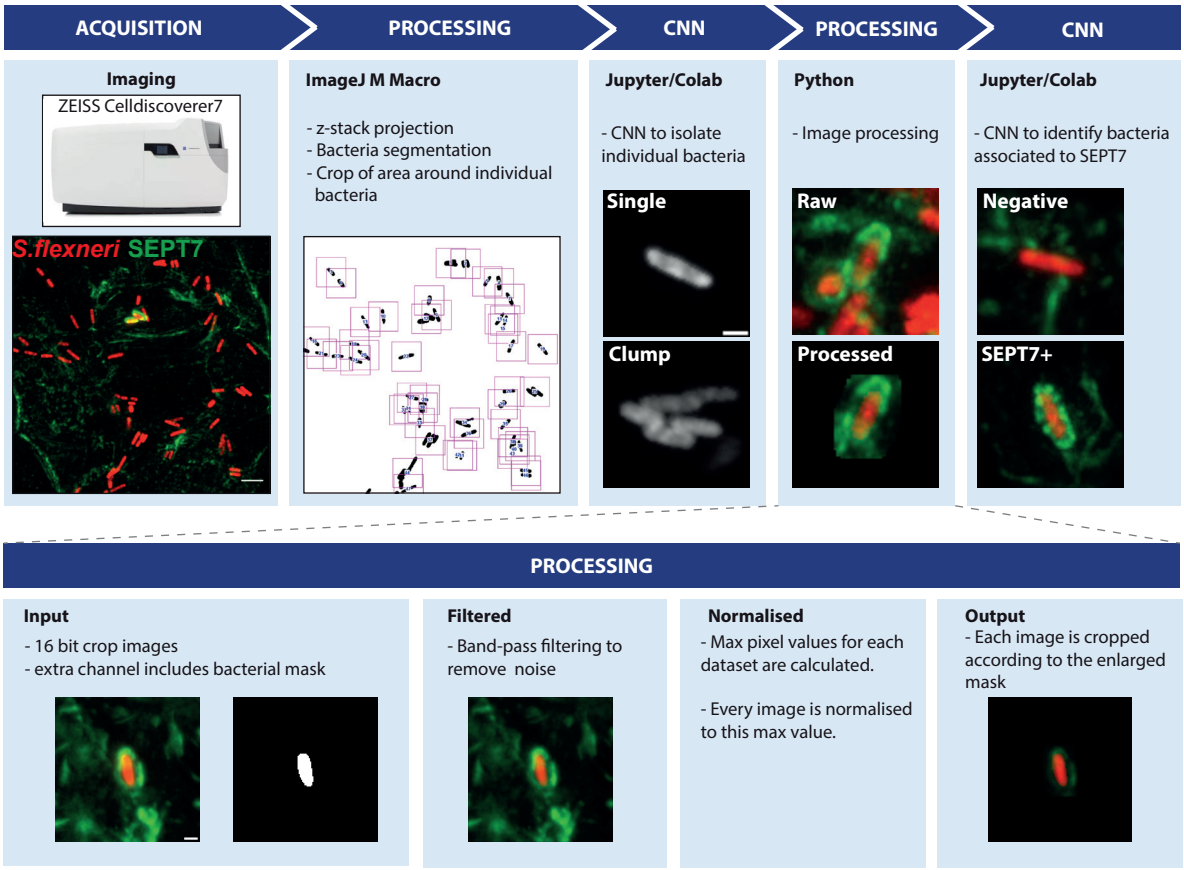
ACQUISITION
PROCESSING
CNN
PROCESSING
CNN
Imaging
ZEISS Celldiscoverer7
S.flexneri SEPT7
ImageJ M Macro
- z-stack projection
- Bacteria segmentation
- Crop of area around individual bacteria
Jupyter/Colab
- CNN to isolate individual bacteria
Single
Clump
Python
- Image processing
Raw
Processed
Jupyter/Colab
- CNN to identify bacteria associated to SEPT7
Negative
SEPT7+
PROCESSING
Input
- 16 bit crop images
- extra channel includes bacterial mask
Filtered
- Band-pass filtering to remove noise
Normalised
- Max pixel values for each dataset are calculated.
- Every image is normalised to this max value.
Output
- Each image is cropped according to the enlarged mask

Figure 4

A

Label	N° of images	Dataset 1	2	3	4
Single bact.	1209	885	0	143	181
Clump	933	253	578	35	67

Dataset 1 and 2: training 80%, validation 20%. Dataset 3 and 4: test.

B

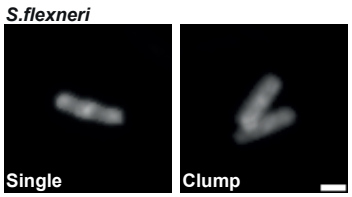

C

Model: "sequential" Total trainable parameters: 25,154

Layer	Output shape	Parameters
Conv2D (1)	(None, 126, 126, 4)	40
MaxPooling2D	(None, 63, 63, 4)	0
Conv2D (2)	(None, 61, 61, 8)	296
MaxPooling2D	(None, 30, 30, 8)	0
Conv2D (3)	(None, 28, 28, 16)	1,168
MaxPooling2D	(None, 14, 14, 16)	0
Conv2D (4)	(None, 12, 12, 32)	4,640
MaxPooling2D	(None, 6, 6, 32)	0
Conv2D (5)	(None, 4, 4, 64)	18,496
MaxPooling2D	(None, 2, 2, 64)	0
Flatten	(None, 256)	0
Dense	(None, 2)	514
Activation	(None, 2)	0

D

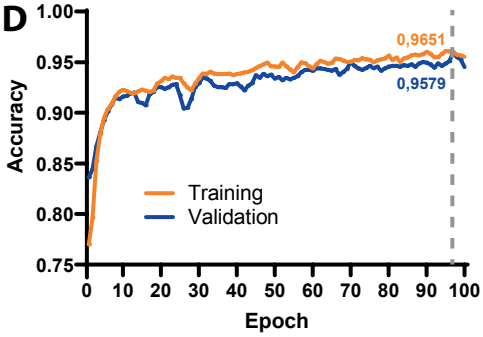

E

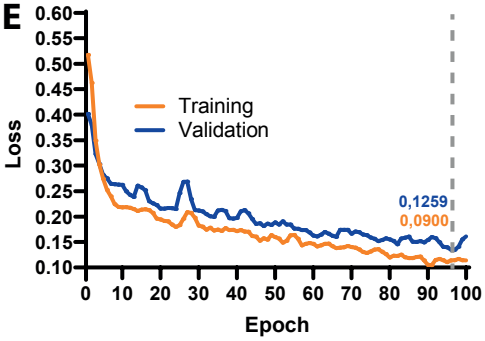

F

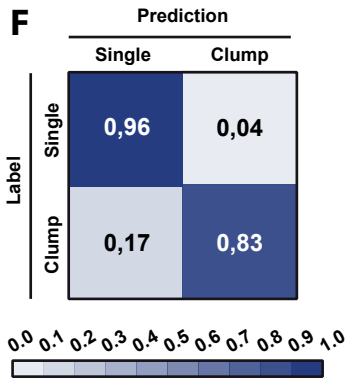

G

	Single	Clump
Precision	0.95	0.90
Recall	0.96	0.83
f1 score	0.95	0.86

H

Label	Total images	Dataset 1	2	3	4	5	6
SEPT7+	1203	43	802	68	47	141	102
Negatives	1498	203	758	29	10	498	0

Training 75%, validation 15%, test: 10%.

I

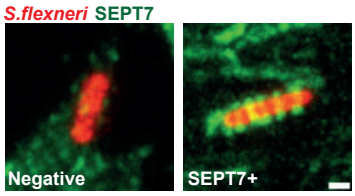

J

Model: "sequential" Total trainable parameters: 56,329

Layer	Output shape	Parameters
Conv2D (1)	(None, 126, 126, 4)	112
Batch_norm (1)	(None, 126, 126, 4)	16
MaxPooling2D (1)	(None, 63, 63, 4)	0
Conv2D (2)	(None, 61, 61, 8)	296
Batch_norm (2)	(None, 61, 61, 8)	32
MaxPooling2D (2)	(None, 30, 30, 8)	0
Conv2D (3)	(None, 28, 28, 16)	1,168
Conv2D (4)	(None, 26, 26, 16)	2,320
Batch_norm (3)	(None, 26, 26, 16)	64
MaxPooling2D (3)	(None, 13, 13, 16)	0
Conv2D (5)	(None, 11, 11, 32)	4,640
Conv2D (6)	(None, 9, 9, 32)	9,248
Batch_norm (4)	(None, 9, 9, 32)	128
MaxPooling2D (4)	(None, 4, 4, 32)	0
Conv2D (7)	(None, 2, 2, 64)	18,496
Batch_norm (5)	(None, 2, 2, 64)	256
MaxPooling2D (5)	(None, 1, 1, 64)	0
Flatten	(None, 64)	0
Dense (1)	(None, 300)	19,500
Activation (1)	(None, 300)	0
Dense (2)	(None, 1)	301
Activation (2)	(None, 3)	0

K

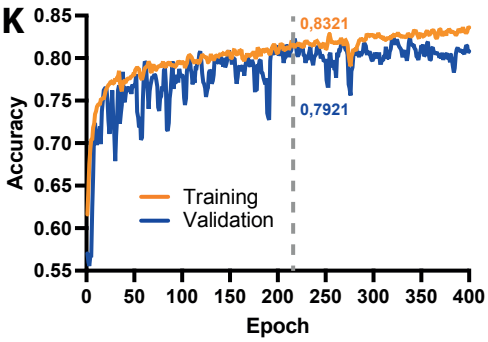

L

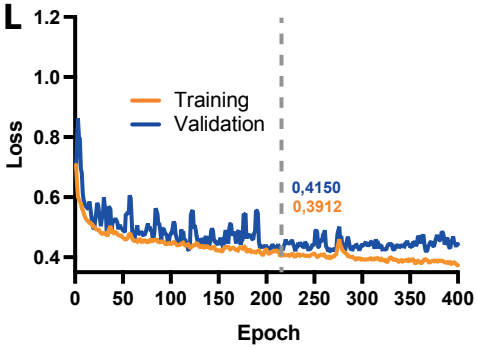

M

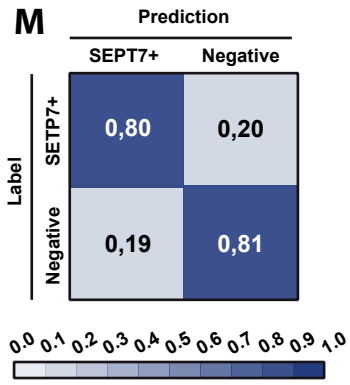

N

	SEPT7+	Negative
Precision	0.78	0.84
Recall	0.80	0.81
f1 score	0.79	0.83

Figure 5

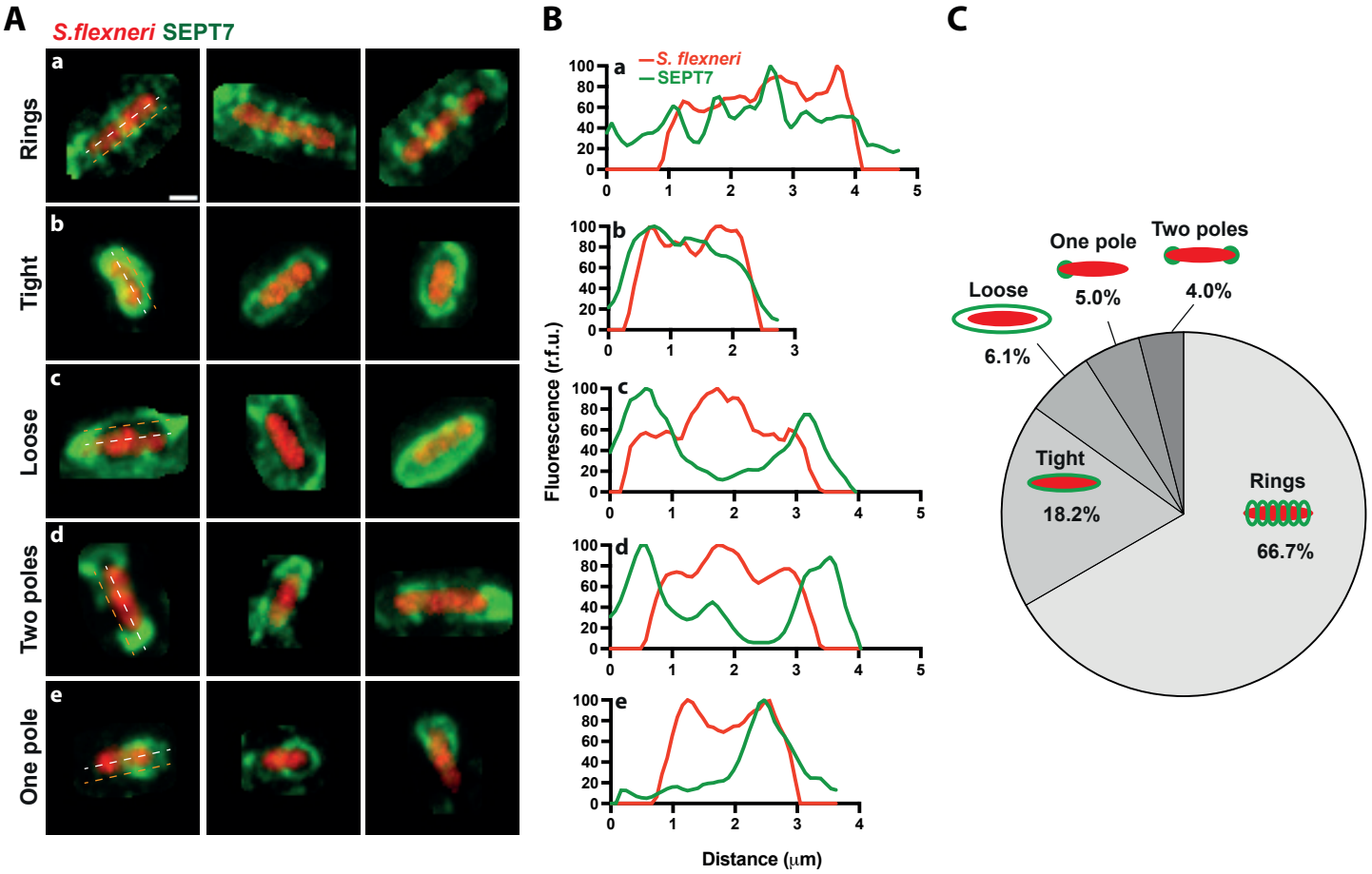
A
S.flexneri SEPT7
Rings
Tight
Loose
Two poles
One pole
a
b
c
d
e
B
S. flexneri
SEPT7
Fluorescence (r.f.u.)
Distance (μm)
C
Loose
6.1%
One pole
5.0%
Two poles
4.0%
Tight
18.2%
Rings
66.7%

Figure 6

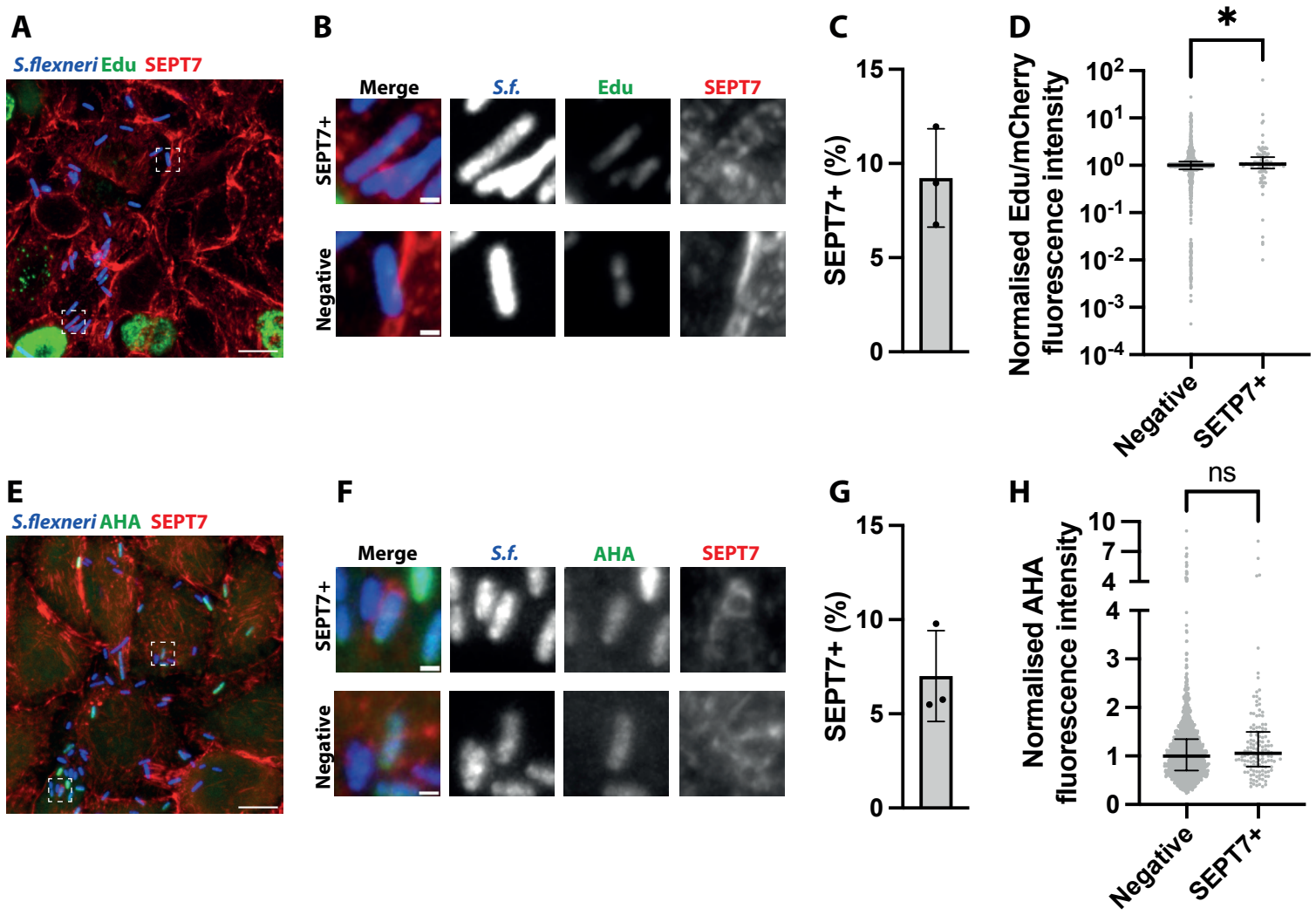
A
S.flexneri Edu SEPT7
B
Merge
S.f.
Edu
SEPT7
SEPT7+
Negative
C
SEPT7+ (%)
15
10
5
0
D
*
Normalised Edu/mCherry fluorescence intensity
10^2
10^1
10^0
10^{-1}
10^{-2}
10^{-3}
10^{-4}
Negative
SETP7+
E
S.flexneri AHA SEPT7
F
Merge
S.f.
AHA
SEPT7
SEPT7+
Negative
G
SEPT7+ (%)
15
10
5
0
H
ns
Normalised AHA fluorescence intensity
10
7
4
4
3
2
1
0
Negative
SEPT7+

Figure 7

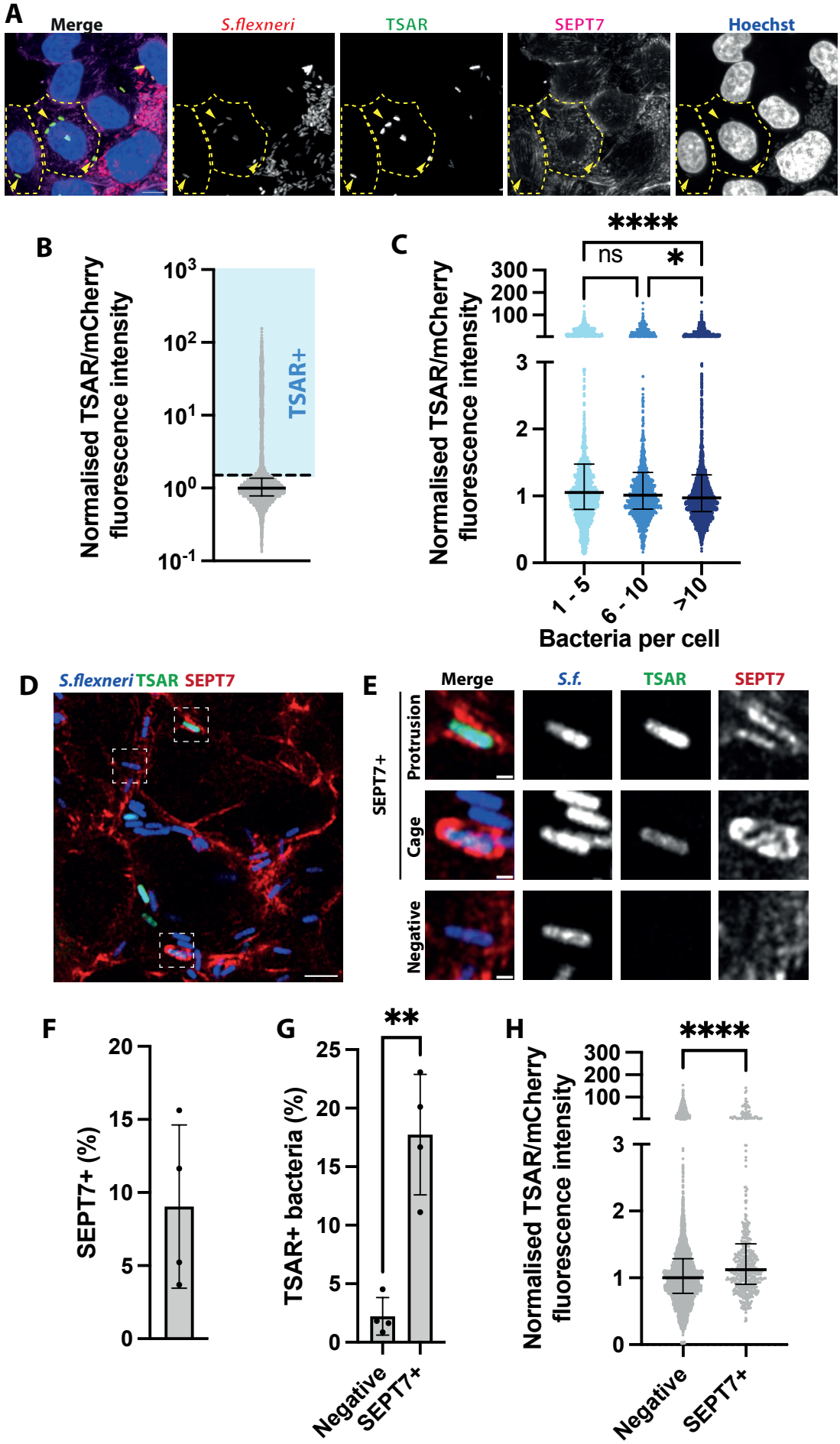
A
Merge
S.flexneri
TSAR
SEPT7
Hoechst
B
Normalised TSAR/mCherry fluorescence intensity
TSAR+
C
****
ns
*
Normalised TSAR/mCherry fluorescence intensity
1 - 5
6 - 10
>10
Bacteria per cell
D
S.flexneri TSAR SEPT7
E
Merge
S.f.
TSAR
SEPT7
SEPT7+
Protrusion
Cage
Negative
F
SEPT7+ (%)
G
**
TSAR+ bacteria (%)
Negative
SEPT7+
H
****
Normalised TSAR/mCherry fluorescence intensity
Negative
SEPT7+